Journal of Non-Newtonian Fluid Mechanics 219 (2015) 1–18

Contents lists available at ScienceDirect

Journal of Non-Newtonian Fluid Mechanics

journal homepage: http://www.elsevier.com/locate/jnnfm

Viscoplastic modeling of granular column collapse with pressure-dependent rheology

Ioan R. Ionescu [a,b,*], Anne Mangeney [c,d], François Bouchut [e], Olivier Roche [f]

[a] LSPM, University Paris-Nord, Sorbonne-Paris-Cité, France
[b] IMAR, Romanian Academy, Bucharest, Romania
[c] Institut de Physique du Globe de Paris, Equipe Sismologie, University Paris-Diderot, Sorbonne Paris Cité, Paris, France
[d] ANGE Team, CEREMA, INRIA, Lab. J. Louis Lions, Paris, France
[e] Université Paris-Est, Laboratoire d'Analyse et de Mathématiques Appliquées, CNRS, UPEM, UPEC, France
[f] Laboratoire Magmas et Volcans, University Blaise Pascal-CNRS-IRD, France

ARTICLE INFO

Article history:
Received 26 October 2014
Received in revised form 20 February 2015
Accepted 23 February 2015
Available online 11 March 2015

Keywords:
Granular collapse
Viscoplastic rheology
Drucker–Prager plasticity
Yield stress
Variable viscosity
Augmented Lagrangian

ABSTRACT

A mechanical and numerical model of dry granular flows is proposed that quantitatively reproduce laboratory experiments of granular column collapse over inclined planes. The rheological parameters are directly derived from the experiments. The so-called $\mu(I)$ rheology is reformulated in the framework of Drucker–Prager plasticity with the yield stress and viscosity $\eta(\|D\|, p)$ depending on both the pressure p and the norm of the strain rate tensor $\|D\|$.

The granular domain, velocities, stress deviator and pressure fields are calculated using a finite element method based on an iterative decomposition–coordination formulation coupled with the augmented Lagrangian method.

2-D simulations using this model well reproduce the dynamics and deposits of collapsing granular columns. The flow is essentially located in a surface layer behind the front, whereas it is distributed over the whole depth near the front where basal sliding occurs. The computed runout distances and slopes of the deposits agree very well with the values found in the experiments.

Using an easily calculated order of magnitude approximation of the mean viscosity during the flow ($\eta = 1$ Pa s here), we show that a Drucker–Prager rheology with a constant viscosity gives results very similar to the $\mu(I)$ rheology and agrees with experimental height profiles, while significantly reducing the computational cost. Within the range of viscosities $0.1 < \eta < 1$ Pa s, the dynamics and deposits are very similar. The observed slumping behavior therefore appears to be mainly due to the flow/no-flow criterion and to the associated strain-independent part of the "flowing constitutive relation" (i.e. related to plastic effects). However, the results are very different when an unrealistically large value of viscosity (10 Pa s) is used.

1. Introduction

The mechanical behavior of dense flows of dry granular material is of paramount importance in very different domains such as geophysics, physics and industry. An increasing number of theoretical and experimental studies are devoted to this subject, in particular to infer the mechanical properties of geophysical granular flows from field observations. Geophysical flows (rock-falls, rock or debris avalanches, etc.) have been simulated mostly using thin layer depth-averaged models to reduce the high computational costs related to the necessary description of the real topography. Besides the prohibitive cost of the computations that would be required to use the equations of mass and momentum conservation without depth-averaging and/or a thin layer approximation, the lack of a well established constitutive relation for these complex natural materials has prevented the development such models for application in real situations. Furthermore, the rheological parameters associated with complex natural materials are generally very hard to measure and the properties of the material may change significantly during the flow, in particular due to fragmentation, segregation or entrainment processes. In this context, a key point for real applications is to use constitutive relations

* Corresponding author at: LSPM, University Paris-Nord, Sorbonne-Paris-Cité, France.
E-mail addresses: ioan.r.ionescu@gmail.com (I.R. Ionescu), mangeney@ipgp.fr (A. Mangeney), francois.bouchut@u-pem.fr (F. Bouchut), O.Roche@opgc.univ-bpclermont.fr (O. Roche).

http://dx.doi.org/10.1016/j.jnnfm.2015.02.006
0377-0257/

with the minimum number of parameters required to describe the mean behavior of the flow. Despite all these difficulties, developing 3D models of granular flows is crucial because certain key processes such as the flow/no-flow transition present in particular in erosion and deposition mechanisms are not adequately handled in thin-layer depth-averaged models. Furthermore 3D structures such as convection cells may play a role in the flow dynamics [1], especially for natural landslides that are intrinsically transient and significantly affected by topographical fluctuations. We refer the reader to numerous reviews [2–5] for a general introduction to granular flows.

Even though granular flows at the laboratory scale may not involve the same physical processes as those acting at the natural scale, they provide a very useful way to investigate and quantify possible mechanisms and scaling laws as well as to test constitutive relations. Moreover, the results of such a small-scale analysis are often assumed to be valid at a large scale. In particular, the transient flows obtained by the release of granular columns at the laboratory scale have been largely used in recent years to investigate granular flow dynamics and deposits. We will simulate here the collapse of granular columns over horizontal and inclined channels as carried out experimentally by Mangeney et al. [6]. These experiments were along the same lines as other granular collapse experiments, mainly performed on horizontal planes in channels (e.g. dam-break) or over unconfined beds [7–14]. Some of them were extended to granular collapse on rigid inclined beds [15,6,11,16] or erodible granular beds [17,6,16]. Efforts to explain the scaling laws obtained in these experiments have either concentrated on thin layer models [18–21], Discrete Element Methods (DEM) [22,23,14,24] or more recently on continuum viscoplastic models [17,25–27].

Many numerical studies have focused on reproducing the experimental scaling laws for granular collapse over horizontal beds, but few quantitative comparisons have been made between simulations and experiments for the flow dynamics and deposits and none have considered the viscoplastic rheology investigated here. Indeed, although all such studies reproduced the scaling laws, they often did not correctly reproduce the runout distance and duration of the flow. While thin layer depth-averaged models based on a Coulomb-type friction well reproduce quantitatively the final deposits for aspect ratios lower than 1 using an empirical friction coefficient slightly higher than the tangent of the friction angle of the involved particles ($\mu = 0.6$), the spreading velocity during the first moments of the collapse is significantly overestimated [18,19,28]. On the other hand, the 2D DEM (based on contact dynamics) proposed by Staron and Hinch [22] strongly overestimates the maximum extent of the deposit (by up to 40%) for dam-break granular collapses even when a very high grain/grain friction coefficient ($\mu_m = 1$) is used. Using a 3D DEM (based on soft particle dynamics), Lacaze et al. [20] reproduced quantitatively a dam-break granular collapse of small lateral width (1 or 2 particles) using a grain/grain friction coefficient of $\mu_m = 0.35$ and an empirical friction coefficient along the lateral wall, which surprisingly varies significantly depending on the size of the granular particles ($\mu_w = 0.15$ or 0.35). Similarly, a 3D DEM (soft particle dynamics) for a wider dam-break granular collapse [24] reproduced quantitatively the dynamics and the deposits observed experimentally with a grain/grain friction coefficient of $\mu_m = 0.5$, a particle–wall friction coefficient of $\mu_w = 0.5$ and an empirical additional dissipation said to be related to the resistance of the grains to rolling along the wall. The runout of an unconfined granular collapse was quantitatively reproduced by Lacaze and Kerswell [25] using a 3D DEM (soft particle dynamics) with a grain/grain friction coefficient of $\mu_m = 0.5$. These results suggest that DEM simulations must be performed in 3D to reproduce quantitatively the experimental collapse of granular columns, even for dam-break configurations.

We propose here alternatively to use a continuum approach to simulate dam-break granular collapse based on viscoplastic constitutive relations in line with recent studies and to quantitatively compare results with those obtained from laboratory experiments. Crosta et al. [17] first simulated horizontal granular collapse using an elastoplastic constitutive relation with a Mohr–Coulomb yield rule involving a constant friction coefficient and a nonassociated flow rule, while maintaining a slight cohesion to avoid numerical problems. They found good agreement with the experimental scaling laws for the deposit, with internal friction angles within a few degrees of the characteristic repose and avalanche angles of the material involved, even though the final maximum thickness of the deposit was slightly underestimated. However, they did not compare the experiments and the simulation in detail during the flow (thickness profiles, front position and velocity, etc.). On the other hand, Lacaze and Kerswell [25], using a 3D DEM, showed that the so-called viscoplastic $\mu(I)$ rheology seemed to hold during the 3D collapse of granular columns, where I is referred to as the inertial number. Note that many studies have shown that the $\mu(I)$ flow law makes it possible to describe a wide range of experimental observations (e.g. GDR MiDi group [3], Silbert et al. [29], Jop et al. [30,31]). More recently, Lagrée et al. [27] compared 2D continuum and DEM (contact dynamics) simulations of granular collapse. In their continuum model, Lagrée et al. [27] prescribed no-slip boundary conditions at the bottom, neglecting possible basal sliding. They showed that for a given parameter set, the continuum and discrete approaches gave very similar results. As already mentioned, the DEMs used by Lagrée et al. [27] and by Staron and Hinch [22] strongly overestimated the runout extent of the deposit observed experimentally. For the selected parameter set, the continuum approach predicted a shorter runout distance than the DEM. In their study, Lagrée et al. [27] found similar scaling laws for both approaches, but they were still much larger than those obtained in the experiments (by more than 20%). The $\mu(I)$ rheology gave better results than a friction law with a constant friction coefficient μ even though, at a small aspect ratio (a = 1.42), their results showed only very slight differences between the two laws, similar to those obtained using $\mu(I)$ with different rheological parameters (see their Fig. 16). These differences are located near the front of the flow, which traveled faster for $\mu = cst$.

For practical applications to natural flows, the possible relevance of a simplified rheology (constant friction and/or constant viscosity) for granular flows over inclined slopes is a critical issue because the three parameters involved in the $\mu(I)$ rheology are very difficult to calibrate in nature and because the small viscosities involved in this rheology may induce prohibitive computational times.

We will focus here on a detailed quantitative comparison of Drucker Prager plasticity models featuring constant and variable viscosity with experimental results on the dynamics and deposits of dam-break granular flows. While former similar simulations were restricted to horizontal planes, we will also investigate granular flows over inclined topography. First, we will present the 2D viscoplastic continuum model developed here (Section 2.1) with the $\mu(I)$ rheology reformulated in a viscoplastic context using Drucker–Prager plasticity (pressure-dependent yield stress) and a variable viscosity. Then, a quantitative comparison between the simulations and laboratory experiments of granular dam-breaks with small aspect ratios (typical of natural landslides) over horizontal and inclined planes will be presented to investigate the capability of the viscoplastic model to reproduce the observations (Section 3). In Section 4, we discuss the influence of the gate and of the frictional boundary conditions. The flow properties (velocity profile, basal sliding, yield limit distribution, yielding surface, stagnant zones, evolution of the horizontal and vertical

layers) obtained from the numerical simulations and their strong heterogeneities within the flow are discussed in Section 5. Finally, in Section 6, the results and their implication in terms of rheology and practical applications are discussed. The appendix provides a short description of the numerical scheme used in the computations.

2. Modeling granular collapse

2.1. Pressure dependent viscoplastic fluids

In contrast with a Newtonian fluid, which cannot sustain a shear stress, a rigid viscoplastic fluid at rest (i.e. no strain rate) can sustain a Cauchy symmetric stress $\boldsymbol{\sigma}$ belonging to a set of admissible rigid stresses. This set is usually defined by a continuous scalar function $F = F(\|\boldsymbol{\sigma}'_0\|, p)$ that describes the flow/no-flow condition, i.e. $F(\|\boldsymbol{\sigma}'_0\|, p) \leqslant 0$ if and only if the fluid is at rest, where $p = -\frac{1}{3}\mathrm{trace}(\boldsymbol{\sigma})$ is the pressure and $\boldsymbol{\sigma}' = p\boldsymbol{I} + \boldsymbol{\sigma}$ is the deviatoric stress. Throughout the paper, $\|\boldsymbol{A}\| = \sqrt{\boldsymbol{A} : \boldsymbol{A}/2}$ denotes the second invariant of a deviator $\boldsymbol{A}$. If the fluid is flowing, then the stress does not belong to the set of admissible rigid stresses and we must define a "flowing constitutive equation". We shall neglect the second order effects to limit our discussion to a subclass of (incompressible) viscoplastic fluids characterized by

$$\mathrm{trace}(\boldsymbol{D}) = 0, \quad \begin{cases} \boldsymbol{\sigma}' = \beta(\|\boldsymbol{D}\|, p)\boldsymbol{D} & \text{if } \boldsymbol{D} \neq 0, \\ F(\|\boldsymbol{\sigma}'\|, p) \leqslant 0 & \text{if } \boldsymbol{D} = 0, \end{cases} \tag{1}$$

where $\boldsymbol{D} = \boldsymbol{D}(\boldsymbol{u}) \equiv (\nabla \boldsymbol{u} + \nabla^T \boldsymbol{u})/2$ is the strain rate tensor and $\boldsymbol{u}$ is the velocity field. Note that in contrast with a classical fluid constitutive equation for a rigid viscoplastic fluid/solid, the function β is discontinuous at $\boldsymbol{D} = 0$.

We will describe here a procedure to define expressions of the constitutive functions $F(\|\boldsymbol{\sigma}'\|, p)$ and $\beta(\|\boldsymbol{D}\|, p)$ such that the model (1) is consistent (i.e. the compatibility conditions of Cazacu and Ionescu [32] are satisfied). One technique is the so-called superposition method (see Cazacu and Ionescu [32]). The main assumption is that the state of stress in the material, $\boldsymbol{\sigma}'$, can be represented as the sum of a viscous (rate-dependent) contribution $\boldsymbol{\sigma}^V$ and a (rate-independent, i.e. depending only on $\boldsymbol{D}/\|\boldsymbol{D}\|$, and not on $\|\boldsymbol{D}\|$) contribution $\boldsymbol{S}$ related to plastic effects,

$$\boldsymbol{\sigma}' = \boldsymbol{\sigma}^V + \boldsymbol{S}. \tag{2}$$

The viscous part of the stress is expressed as for a classical viscous fluid,

$$\boldsymbol{\sigma}^V = 2\eta(\|\boldsymbol{D}\|, p)\boldsymbol{D}, \tag{3}$$

where η is a viscosity coefficient that may depend on $\|\boldsymbol{D}\|$ and p. The viscous contribution $\boldsymbol{\sigma}^V$ must be continuous in $\boldsymbol{D}$ and vanishes for $\boldsymbol{D} = 0$, i.e.

$$\eta(\|\boldsymbol{D}\|, p)\|\boldsymbol{D}\| \to 0, \quad \text{as} \quad \boldsymbol{D} \to 0. \tag{4}$$

We assume that there is flow only if the yield condition, expressed in terms of the plastic stress deviator $\boldsymbol{S}$ and p, is satisfied, i.e. $F(\|\boldsymbol{S}\|, p) = 0$. Since by (1) the strain rate and the plastic deviator are colinear, the strain rate $\boldsymbol{D}$ is given though a "plastic flow rule"

$$\boldsymbol{D} = \|\boldsymbol{D}\|\frac{\boldsymbol{S}}{\|\boldsymbol{S}\|}, \quad \text{with } F(\|\boldsymbol{S}\|, p) \leqslant 0, \quad \|\boldsymbol{D}\|F(\|\boldsymbol{S}\|, p) = 0. \tag{5}$$

Note that the above equation is *rate-independent* and for all admissible plastic stress deviators $\boldsymbol{S}$ we must have $F(\|\boldsymbol{S}\|, p) \leqslant 0$. In order to express $\boldsymbol{S}$ as a function of the strain rate $\boldsymbol{D}$, we must invert the flow rule (5). To do this, we assume that a pressure-dependent yield limit $\kappa = \kappa(p)$ exists such that the flow/no-flow condition $F(\|\boldsymbol{S}\|, p) = 0$ can be represented as $\|\boldsymbol{S}\| = \kappa(p)$, i.e. $F(\|\boldsymbol{\sigma}'\|, p) = \|\boldsymbol{\sigma}'\| - \kappa(p)$. We can now invert the flow rule to obtain

$$\boldsymbol{S} = \kappa(p)\frac{\boldsymbol{D}}{\|\boldsymbol{D}\|}. \tag{6}$$

Note that in contrast with the viscous contribution $\boldsymbol{\sigma}^V$, the above stress–strain rate relation is not continuous in $\boldsymbol{D}$, and $\boldsymbol{S}$ does not vanish necessarily for $\boldsymbol{D} = 0$. Following the stress decomposition we obtain the constitutive scalar function $\beta(\|\boldsymbol{D}\|, p) = 2\eta(\|\boldsymbol{D}\|, p) + \kappa(p)/\|\boldsymbol{D}\|$. Now we can compute $\|\boldsymbol{\sigma}'\| = 2\eta(\|\boldsymbol{D}\|, p)\|\boldsymbol{D}\| + \kappa(p)$ and (1) reads

$$\mathrm{trace}(\boldsymbol{D}) = 0, \quad \begin{cases} \boldsymbol{\sigma}' = 2\eta(\|\boldsymbol{D}\|, p)\boldsymbol{D} + \kappa(p)\frac{\boldsymbol{D}}{\|\boldsymbol{D}\|} & \text{if } \boldsymbol{D} \neq 0, \\ \|\boldsymbol{\sigma}'\| \leqslant \kappa(p) & \text{if } \boldsymbol{D} = 0. \end{cases} \tag{7}$$

This formula clearly represents the decomposition of the deviatoric stress as a sum of a rate-dependent viscous term and a rate-independent plastic term with yield stress. We can rewrite this relation in a different form by expressing the strain rate $\boldsymbol{D}$ as a function of the stress deviator (see also [33,28]):

$$\boldsymbol{D} = \frac{1}{2\eta(\|\boldsymbol{D}\|, p)}\left[1 - \frac{\kappa(p)}{\|\boldsymbol{\sigma}'\|}\right]_+ \boldsymbol{\sigma}', \tag{8}$$

where $[x]_+ = \max(0, x)$ is the positive part. The above expression was used by Perzyna [34] and Duvaut Lions [35] to extend inviscid plastic models to account for rate effects (viscoplastic regularization method).

For $\kappa(p) \equiv 0$ the plastic effects vanish and (7) reduces to a viscous fluid model. For example, if η is independent of $\|\boldsymbol{D}\|$ and p, (7) reduces to the incompressible Navier–Stokes model. If the plastic effects are present then different choices of yield limit $\kappa(p)$ can be considered. For constant κ (i.e. $\kappa(p) \equiv \kappa_0$ pressure-independent plasticity) we deal with the Von-Mises plasticity criterion $\|\boldsymbol{\sigma}'\| \leqslant \kappa_0$, introduced to describe the plasticity of metals. If η is constant (independent of $\|\boldsymbol{D}\|$ and p), the constitutive Eq. (7) is the classical *Bingham* model (see [2]).

In this paper we consider the yield limit κ to be linearly dependent on the pressure p, a condition referred to as the Drucker–Prager plasticity (flow/no-flow) criterion (see [36]):

$$\kappa(p) = \kappa_0 + \mu_s p, \tag{9}$$

where κ_0 is the cohesion and $\mu_s = \tan(\delta_s)$, with δ_s the internal frictional angle. This yield criterion was constructed as a simplification of the Mohr–Coulomb plasticity criterion.

Here we will use two different models, one with a constant viscosity η (i.e. independent of $\|\boldsymbol{D}\|$ and p) that we will call the "constant viscosity model" (or the Drucker–Prager fluid), and the other with a variable viscosity $\eta(\|\boldsymbol{D}\|, p)$, chosen to get the model proposed by Jop et al. [31] and the inertial number I. The inertial number I, which is the square root of the Savage number or of the Coulomb number introduced by Savage [37] and Ancey et al. [38], respectively, can be interpreted as the ratio between two timescales: the inertial microscopic timescale of particle rearrangement $d/\sqrt{p/\rho_s}$ (where d is the grain diameter and ρ_s is the grain density) and a macroscopic strain rate time scale ($1/\|\boldsymbol{D}\|$), i.e.

$$I = \frac{2\|\boldsymbol{D}\|d}{\sqrt{p/\rho_s}}. \tag{10}$$

Note that this equation is meaningful here only if we assume $p > 0$. As proposed by [31], we introduce variable friction

$$\mu(I) = \mu_s + \frac{\mu_2 - \mu_s}{1 + I_0/I}, \tag{11}$$

where I_0 is a dimensionless constant and $\mu_2 \geqslant \mu_s$ is the limiting value of the friction coefficient for large I. Then the $\mu(I)$ rheology proposed in [31] can be written

$$\text{trace}(\boldsymbol{D}) = 0, \quad \begin{cases} \boldsymbol{\sigma}' = \mu(I) p \frac{\boldsymbol{D}}{\|\boldsymbol{D}\|} & \text{if } \boldsymbol{D} \neq 0, \\ \|\boldsymbol{\sigma}'\| \leqslant \mu(0) p & \text{if } \boldsymbol{D} = 0. \end{cases} \tag{12}$$

It can be identified with the constitutive Eq. (7) by considering the Drucker–Prager plasticity (9) with vanishing cohesion ($\kappa_0 = 0$) and

$$\beta(\|\boldsymbol{D}\|, p) = \frac{\mu(I) p}{\|\boldsymbol{D}\|}, \tag{13}$$

or equivalently by taking the specific dependence of the viscosity η on $\|\boldsymbol{D}\|$ and p given by $2\eta(\|\boldsymbol{D}\|, p)\|\boldsymbol{D}\| = (\mu(I) - \mu_s)p$, i.e. with (11),

$$\eta(\|\boldsymbol{D}\|, p) = \frac{(\mu_2 - \mu_s)p}{2\|\boldsymbol{D}\| + \frac{I_0}{k}\sqrt{p}}, \tag{14}$$

where $k = d\sqrt{\rho_s}$. Note that this viscosity η, corresponding to the decomposition (7), differs from the "effective viscosity" of [31] which is $\beta/2$, in relation to the decomposition (1).

2.2. Experimental setup

Let us describe briefly the granular collapse experiments of Mangeney et al. [6]. The experimental setup consists of a narrow channel between plexiglass walls with a spacing of $W = 10$ cm (around 140 particles). The planar channel is 3 m long with possible inclination angles θ varying from horizontal up to 30° (Fig. 1). A rectangular granular mass of thickness $h_0 = 14$ cm (around 200 particles) and of down-slope length $r_0 = 20$ cm (around 286 particles), i.e. an aspect ratio $a = h_0/r_0 = 0.7$, is released from a reservoir at time $t = 0$ s by opening a gate. The glass beads are subspherical, cohesionless and highly rigid with a diameter $d = 0.7 \pm 0.1$ mm. They flow down an inclined channel, roughened by gluing a layer of the same beads on its surface. The particle density $\rho_s = 2500\ \text{kg m}^{-3}$ and volume fraction $\nu = 0.62$ of the mass were estimated, giving an apparent flow density of

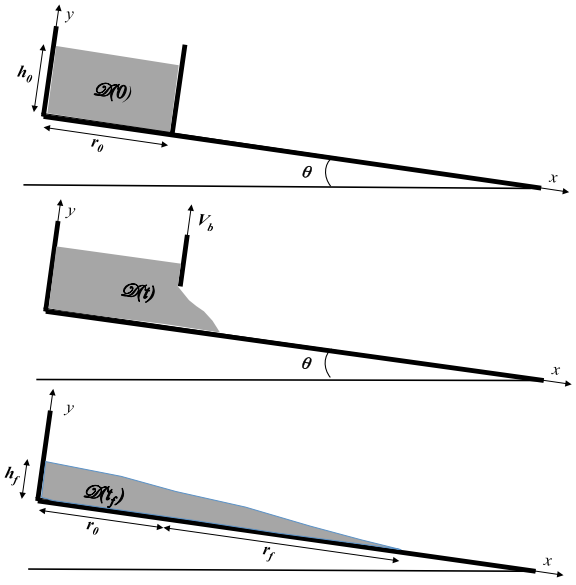

Fig. 1. Experimental setup: morphometric and control parameters measured in the experiments. The initial mass (light gray) with initial thickness $h_0 = 14$ cm and width $r_0 = 20$ cm is released on a plane with inclination θ by opening very rapidly a gate at time $t = 0$ s. It forms a deposit with a length r_f from r_0 (runout distance), and a final maximum thickness h_f. The gate is represented by a thick line perpendicular to the plane.

$\rho = \nu\rho_s = 1550\ \text{kg m}^{-3}$, the value used in (15). The parameter k in the variable viscosity $\eta(\|\boldsymbol{D}\|, p)$ rheology (19) is $k = 0.035\ \text{kg}^{1/2}\,\text{m}^{-1/2}$.

The length of the deposit r_f measured from the front of the initial mass located at $x = 0$, i.e. the runout distance, and the final thickness of the deposit at the back wall h_f were systematically recorded as well as the time at which the front stopped t_f. The profiles of the granular mass were measured as a function of time using a high-speed camera.

In the experiments, a gate is removed at the initial time to release the granular mass. Gate removal is simulated here by considering a lifting velocity $V_b = h_0/t_b = 2.3\ \text{m s}^{-1}$ (where $t_b = 0.06$ s is the lifting time) as measured in the experiments of Mangeney et al. [6] and Farin et al. [16]. In the numerical scheme, the barrier is considered as a simple rigid boundary under an assumed no penetration condition ($\boldsymbol{u} \cdot \boldsymbol{n} = 0$), however the position of the gate changes at each time step. For the sake of simplicity, we neglect here the friction between the gate and the granular material, even though friction is expected to occur as shown for example in Figs. 6 and 14 of [6] (see Section 4.1 for a detailed analysis of the gate effect).

2.3. Problem statement

To model the granular collapse experiment described above, we consider here the equations describing the in-plane flow of a rigid viscoplastic fluid over the time interval $(0, T), T > 0$ in a domain $\mathcal{D}(t) \subset \mathbb{R}^2$ with a smooth boundary $\partial\mathcal{D}(t)$.

The notation $\boldsymbol{u}$ stands for the 2-D velocity field ($\boldsymbol{u} = (u_x, u_y), u_z = 0$) and $\boldsymbol{\sigma}$ for the 3-D stress tensor field ($\sigma_{xz} = \sigma_{yz} = 0$), while $p = -\text{trace}(\boldsymbol{\sigma})/3$ is the pressure and $\boldsymbol{\sigma}' = \boldsymbol{\sigma} + pI$ the in-plane stress deviator tensor ($\sigma'_{xz} = \sigma'_{yz} = \sigma'_{zz} = 0$).

Mass and momentum conservation. The momentum balance law (in the Eulerian coordinates) reads

$$\rho\left(\frac{\partial \boldsymbol{u}}{\partial t} + (\boldsymbol{u} \cdot \nabla)\boldsymbol{u}\right) - \textbf{div}\ \boldsymbol{\sigma}' + \nabla p = \rho \boldsymbol{f} \quad \text{in } \mathcal{D}(t), \tag{15}$$

where $\rho > 0$ is the mass density distribution and $\boldsymbol{f}$ denotes the body forces (gravity for our purpose). Since we are dealing with an incompressible fluid, we have

$$\text{div}\ \boldsymbol{u} = 0 \quad \text{in } \mathcal{D}(t). \tag{16}$$

The viscoplastic fluid domain $\mathcal{D}(t)$ is transported with the fluid as

$$\frac{\partial 1_{\mathcal{D}(t)}}{\partial t} + \boldsymbol{u} \cdot \nabla 1_{\mathcal{D}(t)} = 0, \tag{17}$$

where $1_{\mathcal{D}(t)}$ is the characteristic function of the domain.

Constitutive laws. We will now consider the constitutive Eq. (7) with $\boldsymbol{D} = \boldsymbol{D}(\boldsymbol{u}) \equiv (\nabla\boldsymbol{u} + \nabla^T\boldsymbol{u})/2$ and with Drucker–Prager plasticity (9) with vanishing cohesion ($\kappa_0 = 0$). Two different choices of the viscosity η will be analyzed: the constant viscosity model ($\eta = cst$)

$$\text{trace}(\boldsymbol{D}) = 0, \quad \begin{cases} \boldsymbol{\sigma}' = 2\eta\boldsymbol{D} + \mu_s p \frac{\boldsymbol{D}}{\|\boldsymbol{D}\|} & \text{if } \boldsymbol{D} \neq 0, \\ \|\boldsymbol{\sigma}'\| \leqslant \mu_s p & \text{if } \boldsymbol{D} = 0, \end{cases} \tag{18}$$

and the variable viscosity model with η given by (14),

$$\text{trace}(\boldsymbol{D}) = 0, \quad \begin{cases} \boldsymbol{\sigma}' = 2\frac{(\mu_2 - \mu_s)p}{2\|\boldsymbol{D}\| + \frac{I_0}{k}\sqrt{p}}\boldsymbol{D} + \mu_s p \frac{\boldsymbol{D}}{\|\boldsymbol{D}\|} & \text{if } \boldsymbol{D} \neq 0, \\ \|\boldsymbol{\sigma}'\| \leqslant \mu_s p & \text{if } \boldsymbol{D} = 0, \end{cases} \tag{19}$$

with $k = d\sqrt{\rho_s}$, which is equivalent to the $\mu(I)$ rheology (12). Note that the division of $\boldsymbol{\sigma}'$ and p by ρ_s involves the dynamic viscosity and pressure $\eta/\rho_s, p/\rho_s$. Consequently any of the previous rheologies can be written in terms of the dynamic variables

$\boldsymbol{\sigma}'/\rho_s, p/\rho_s, \eta/\rho_s$. In this way the grain density ρ_s is eliminated and only the rheological parameters $\mu_s, \mu_2, I_0/d$ remain.

Boundary and initial conditions. In order to complete the above equations with boundary conditions we assume that $\partial\mathcal{D}(t)$ is divided into two disjoint parts $\partial\mathcal{D}(t) = \Gamma_b(t) \cup \Gamma_s(t)$. On the boundary $\Gamma_b(t)$, the fluid is in contact with a rigid body through the Coulomb friction law

$$\boldsymbol{u}\cdot\boldsymbol{n} = 0, \quad \begin{cases} \boldsymbol{\sigma}_T = -\mu_C[-\sigma_n]_+ \frac{\boldsymbol{u}_T}{|\boldsymbol{u}_T|} & \text{if } \boldsymbol{u}_T \neq 0, \\ |\boldsymbol{\sigma}_T| \leqslant \mu_C[-\sigma_n]_+ & \text{if } \boldsymbol{u}_T = 0, \end{cases} \tag{20}$$

where μ_C is the Coulomb friction coefficient at the boundary, $\boldsymbol{n}$ stands for the outward unit normal on $\partial\mathcal{D}(t)$ and we adopt the following notation for the tangential and normal decomposition of the velocity field $\boldsymbol{u}$ and surface stresses $\boldsymbol{\sigma n}$

$$\boldsymbol{u} = u_n\boldsymbol{n} + \boldsymbol{u}_T, \quad \text{with } u_n = \boldsymbol{u}\cdot\boldsymbol{n}, \quad \boldsymbol{\sigma n} = \sigma_n\boldsymbol{n} + \boldsymbol{\sigma}_T \quad \text{with } \sigma_n = \boldsymbol{\sigma n}\cdot\boldsymbol{n},$$

where $\boldsymbol{\sigma} = \boldsymbol{\sigma}' - p\boldsymbol{I}$. Note that our boundary conditions at the bottom are different from previous studies of continuum viscoplastic simulations of granular collapse that imposed a no-slip condition [17,27], corresponding to the limit $\mu_C \to \infty$.

On the (unknown) free surface boundary $\Gamma_s(t)$, which is computed from the advection Eq. (17), we impose a stress free condition:

$$\boldsymbol{\sigma n} = 0 \quad \text{on} \quad \Gamma_s(t). \tag{21}$$

The initial conditions are given by

$$\boldsymbol{u}|_{t=0} = 0, \quad \mathcal{D}(0) = \mathcal{D}_0. \tag{22}$$

Finally the problem is to find the domain $\mathcal{D}(t)$, the velocity field $\boldsymbol{u}(t)$, the pressure $p(t)$ and the deviatoric stress tensor $\boldsymbol{\sigma}'(t)$ satisfying Eqs. (15)–(18) (or (19)) with the boundary and initial conditions (20)–(22).

2.4. Rheological parameters

The parameters used in the model, which must be derived from the experiments, are: μ_s, μ_2 and I_0 for the $\eta(\|\boldsymbol{D}\|, p)$ rheology (19) and μ_s and η for the constant viscosity rheology (18). For the two rheologies, we must impose the friction at the bed μ_b and the friction at the plexiglass wall at the back of the reservoir μ_w. Note that as the simulations are 2D (downslope/vertical directions), the model does not simulate friction at the two lateral walls bordering the channel. This effect is only accounted for empirically in the effective friction coefficients as described bellow. In Mangeney et al. [6], the repose angle $\theta_r = 23.5^\circ \pm 0.5^\circ$ ($\mu_r = \tan\theta_r = 0.43 \pm 0.01$) and the avalanche angle $\theta_a = 25.5^\circ \pm 0.5^\circ$ ($\mu_a = \tan\theta_a = 0.48 \pm 0.01$) of the material were measured by adding material on top of a pile at a small rate and measuring the angle of the pile with respect to the horizontal after and before an avalanche, respectively.

The glass beads used by [6] are very similar to those used by Pouliquen and Forterre [39] and Jop et al. [30] and are expected to be characterized by the same rheological parameters. As explained in Pouliquen and Forterre [39], the friction coefficients in the $\mu(I)$ rheology can be obtained by fitting the curve $h_{\text{stop}}(\theta)$, where h_{stop} is the maximum thickness of deposit resulting from steady uniform flows. The resulting minimum and maximum friction angles fitted by Pouliquen and Forterre [39] and Jop et al. [30] are about $\theta_s = 21^\circ$ ($\mu_s = 0.38$) and $\theta_2 = 32.8^\circ$ ($\mu_2 = 0.64$), respectively. Slightly higher friction angles were observed in the experiments of [6] (compare Fig. 5 of [6] and Fig. 3 of [39]). This may result from the width of the channel that is much smaller ($W = 10$ cm) in [6] than in [39] ($W = 70$ cm). Consequently, the effect of the lateral walls can be modeled as an additional friction coefficient with a maximum value of the order of $\mu_w h/W$ where μ_w is the grain/wall friction and h is the thickness of the flowing layer (see Eq. (1) of Taberlet et al. [40] or Eq. (4.5) of Jop et al. [30]).

Assuming that the beads slip against the lateral side walls and that the induced stress is pure solid friction with a constant coefficient of friction μ_w, Jop et al. [30] measured $\mu_w = \tan(10.5^\circ) = 0.18$. We therefore chose $\mu_w = \tan(10.5^\circ) = 0.18$ for the friction on the plexiglass wall at the back of the reservoir. Note that this value is also consistent with the small grain/wall friction in the DEM of Lacaze et al. [14] but much smaller than the value used by Girolami et al. [24]. In [6], as the maximum flowing thickness is about 0.05 m, the additional friction contribution related to the walls should be at most $0.18 \times 0.05/0.1 = 0.09$, while in Pouliquen and Forterre [39] this additional friction would be $0.18 \times 0.01/0.7 = 0.0026$ (see their Fig. 10 for an approximation of the flowing depth). Therefore we expect a difference in the friction coefficients of about 0.1 between Mangeney et al. [6] and Pouliquen and Forterre [39]. As a result, friction coefficients corresponding to the experiments in [6] should be $\mu_s \simeq 0.38 + 0.1 = 0.48 = \tan(25.6^\circ)$ and $\mu_2 \simeq 0.64 + 0.1 = 0.74 = \tan(36.5^\circ)$. Finally, we chose here $\mu_s = \tan(25.5^\circ) \simeq 0.48$ and $\mu_2 = \tan(36^\circ) \simeq 0.73$.

The value of $I_0 = 0.279$ is taken from Pouliquen and Forterre [39]. Our values of the $\eta(\|\boldsymbol{D}\|, p)$ parameters (i.e. $\mu(I)$) are summarized in Table 1 and are consistent with those deduced from a DEM by Lacaze and Kerswell [25] that reproduced quantitatively the scaling laws for axisymmetric glass beads collapses ($\mu_s \simeq 0.4, \mu_2 \simeq 0.7$ and $I \simeq 0.3$). Lagrée et al. [27] used $\mu_s = 0.32, \mu_2 = 0.6$ and $I = 0.4$, overestimating the runout distances of experimental granular collapses.

Another parameter that must be chosen is the frictional coefficient μ_C involved in the boundary condition (20), modeling the contact with the surrounding rigid walls. At the bed, $\mu_C = \mu_b$ is the basal friction coefficient and along the wall at the back of the reservoir, $\mu_C = \mu_w$ is the wall friction coefficient. As the basal roughness was provided by gluing a single layer of the same particles to the channel bed, we chose the same friction coefficient at the basal surface as for the internal friction $\mu_b = \mu_s = \tan(25.5^\circ)$.

To speed up the calculation, we must impose a minimum value of the viscosity $\eta = 0.1$ Pa s (i.e. a kinematic viscosity ν of 4–6×10^{-5} m^2 s^{-1}) for both rheologies. This is necessary with the augmented Lagrangian method, even if the problem can be well-posed (at least in the Bingham case) without viscosity [41,42]. The values of this threshold viscosity and the constant viscosity η are discussed in Section 3.

3. Variable viscosity versus constant viscosity

We will now describe some of the numerical settings we used in the numerical simulations (see Appendix A for a brief description of the numerical scheme). The time step was chosen to be between $\Delta t = 0.0005$ s and $\Delta t = 0.001$ s, while the edge size of the mesh is between $h_{\min} = 0.0033$ m and $h_{\max} = 0.01$ m. Concerning the remeshing process, we used a variable metric/Delaunay automatic meshing algorithm (see [43]) such that the finest meshes are located in the zones of low pressure and high velocity (see the blue mesh in Fig. 6). We also checked that the mass loss during the

Table 1
Rheological parameters.

μ_s (δ_s)	μ_b (δ_b)	μ_w (δ_w)	μ_2 (δ_2)	I_0	k
0.48 (25.5°)	0.48 (25.5°)	0.18 (25.5°)	0.73 (36°)	0.279	0.035 kg$^{1/2}$ m$^{-1/2}$

simulations was very small (smaller than 0.8%). The removal of the barrier (gate) was simulated by a moving frictionless boundary condition (see Section 4.1 for details and the gate influence).

3.1. Collapse over a horizontal plane $\theta = 0^\circ$

Fig. 2 shows that the model with variable viscosity $\eta(\|\boldsymbol{D}\|, p)$ well reproduces the shape of the granular mass during its spreading over a horizontal plane, with rheological parameters directly derived from the experiments. The colors, representing the norm of the velocity, show that the flow is concentrated only in a shallow sub-domain near the free surface as observed in the experiments and as obtained in the numerical simulations of Crosta et al. [17], Lacaze et al. [14,25] and Lagrée et al. [27]. The computed runout distance r_f and the slope of the deposit are in very good agreement with the experiments while the spreading of the mass is slightly faster during the flow. This was also the case in the discrete element simulation of Lagrée et al. [27] (their Fig. 4) when compared to their experiments. The front is slightly more rounded in our simulation than in the experiments, an effect even more pronounced in the simulation of Crosta et al. [17] (see their Fig. 1a). The thickness of the mass near the back wall decreases slightly in the simulations while it stays constant in the experiments. Fig. 2 shows that already at $t = 0.06$ s, the velocity near the upper part of the back wall is non-zero. As a result, the final maximum thickness of the deposit h_f is about 10% smaller than in the experiments. Similar results were obtained in the continuum and DEM simulations of Crosta et al. [17] (their Fig. 6) and Lacaze et al. [14] (their Figs. 4, 6 and 7), respectively. In our simulation, at time $t = 0.76$ s, the maximum velocity norm is lower than 0.03 m/s and at $t_f = 1.02$ s an equilibrium configuration is reached. Over this long period of time $t \in [0.76, 1.02]$ s many slow flow events occur, changing very slightly the shape of the granular mass before the granular material reaches the final equilibrium state. These processes are also observed in the experiments.

Fig. 3 shows that the viscosity varies from 0.1 Pa s (minimum threshold viscosity in the model) at the free surface to about 1.5 Pa s near the bed (see Eq. (14)). For example, the viscosity within the flowing layer at $t = 0.3$ s is $0.1 < \eta < 0.7$ Pa s. The small viscosity at the free surface is directly related to the low pressure

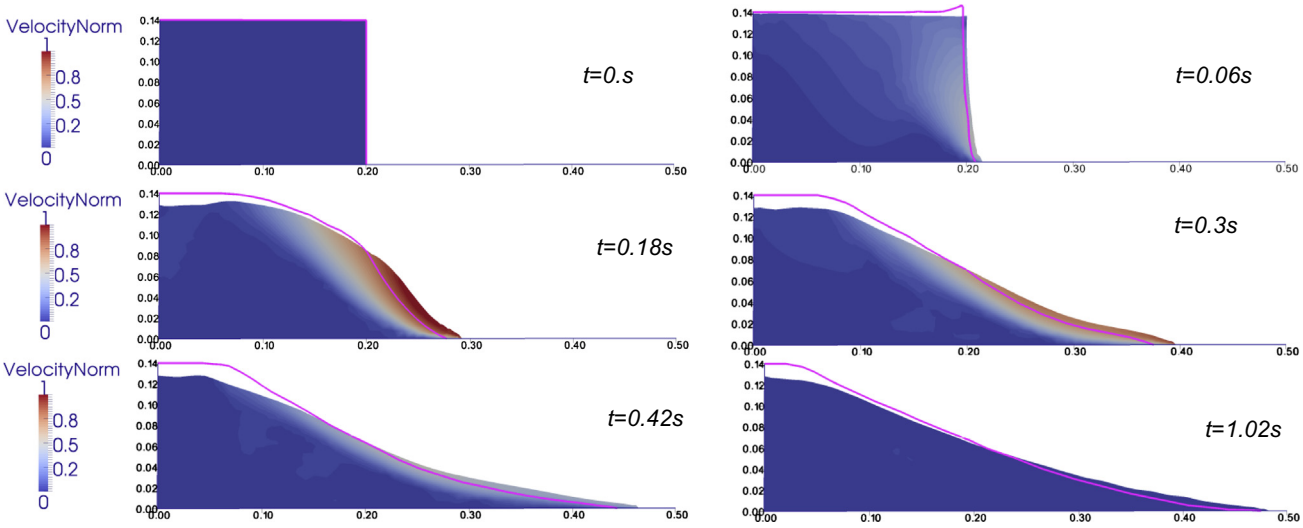

Fig. 2. Simulation using variable viscosity $\eta(\|\boldsymbol{D}\|, p)$ (i.e. $\mu(I)$): Comparison of the simulated granular mass and the experimental results (pink line) at different times for granular collapse over a horizontal plane ($\theta = 0^\circ$). The colors represent the distribution of the norm of the computed velocity field $|\boldsymbol{u}|$ (in m/s). (For interpretation of the references to color in this figure legend, the reader is referred to the web version of this article.)

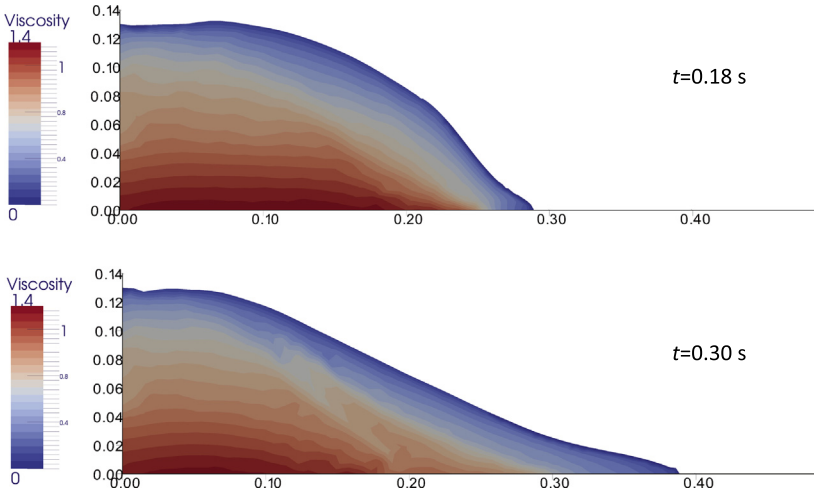

Fig. 3. Viscosity (in Pa s) calculated with the $\mu(I)$ rheology at different times for granular collapse over a horizontal plane ($\theta = 0^\circ$).

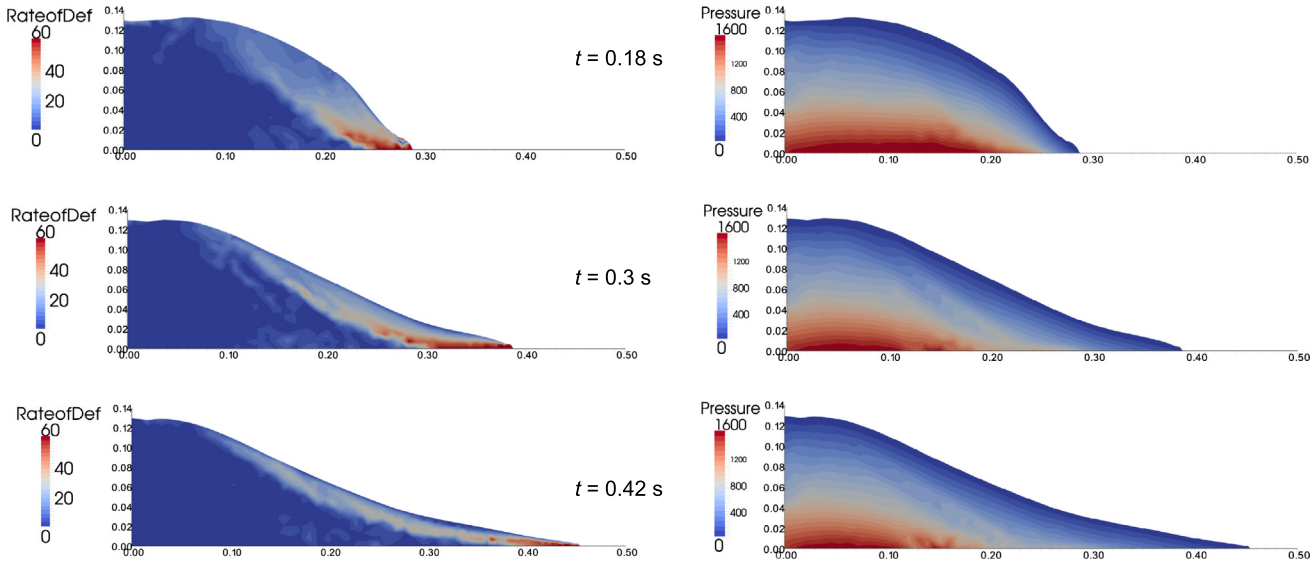

Fig. 4. Strain rate $\|\boldsymbol{D}\|$ in s^{-1} (left column) and pressure p in Pa (right column), calculated with variable viscosity $\eta(\|\boldsymbol{D}\|, p)$ (i.e. $\mu(I)$) at different times for granular collapse over a horizontal plane $\theta = 0°$.

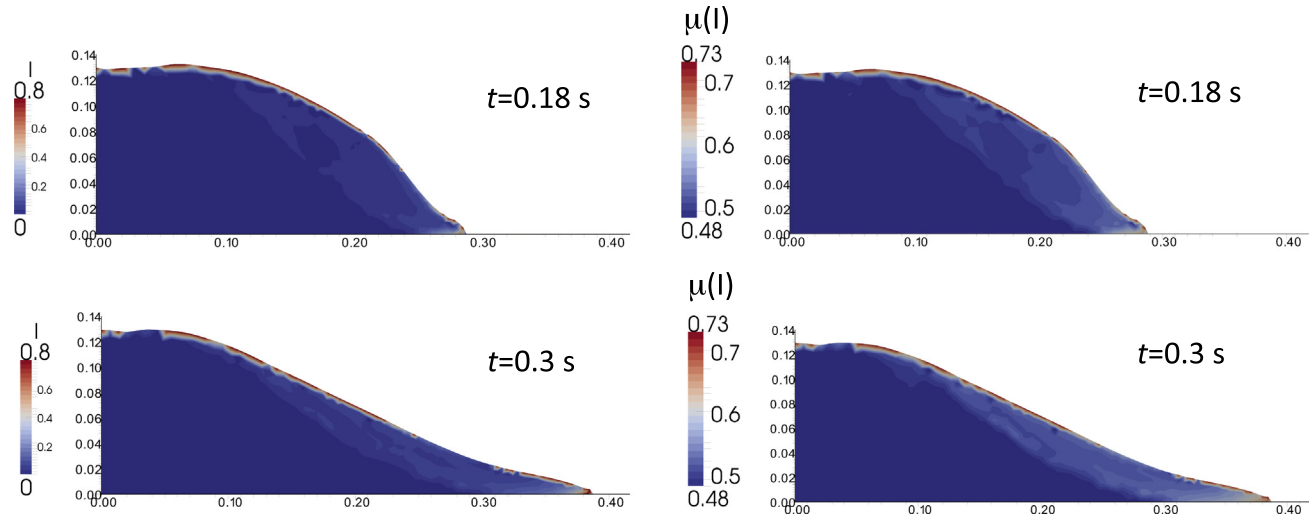

Fig. 5. Values of I and $\mu(I)$ at different times for granular collapse over a horizontal plane ($\theta = 0°$).

in this zone (Fig. 4 right column). While the pressure distribution is quite regular within the flowing region, the strain rate is concentrated near the front and near the bed (Fig. 4 left column). Its maximum value is around $70\,s^{-1}$, so that the first term in the denominator of Eq. (14) is lower than $140\,s^{-1}$. The pressure is already about 200 Pa near the front, which gives a second term in the denominator of (14) equal to about $112\,s^{-1}$ near the front. As a result, in regions of high strain rate, such as near the front, the viscosity is related to both the strain rate and pressure values. At other locations, the first term is much smaller than the second term and the strain rate can be neglected in the viscosity formula (14). Interestingly, while the strain rate is quite localized, the viscosity varies smoothly in the flowing region. The smooth increase in pressure with depth seems to dominate the viscosity variation. This suggests that the strain rate can be neglected in (14), giving

$$\eta \simeq (\mu_2 - \mu_s)\frac{k}{I_0}\sqrt{p}. \tag{23}$$

This approximation is equivalent to linearizing the $\mu(I)$ law (11) for small I,

$$\mu(I) \simeq \mu_s + (\mu_2 - \mu_s)\frac{I}{I_0}. \tag{24}$$

The order of magnitude of the viscosity can be simply obtained from Eq. (14) without performing the simulation, from only the initial thickness of the granular column h_0, the grain diameter and density and the parameters of the $\mu(I)$ rheology. Indeed, taking pressure $p = \rho_s g h_0/2 = 2500 \times 9.81 \times 0.07 = 1716$ Pa and assuming that the flowing layer has a thickness of about the half the initial thickness, that velocity $u = \sqrt{g h_0} \simeq 1.17\ m\,s^{-1}$ (see Fig. 9 of [6]) and that the strain rate $\|\boldsymbol{D}\| = u/(h_0/2) \simeq 17\ s^{-1}$, Eq. (14) gives a viscosity $\eta \simeq 1.2$ Pa s. Note that, for this calculation, the strain rate in Eq. (14) is negligible.

When looking at I and $\mu(I)$, the results are more difficult to interpret in terms of dissipation than when looking at the viscosity (Fig. 5). The inertial number I varies only slightly between zero in the static region and less than 0.1 in most of the flowing region, except near the front and close to the free surface where it reaches values of about 0.8. Near the free surface, I is not well defined because the pressure is equal to zero (see Eq. (10)). These values

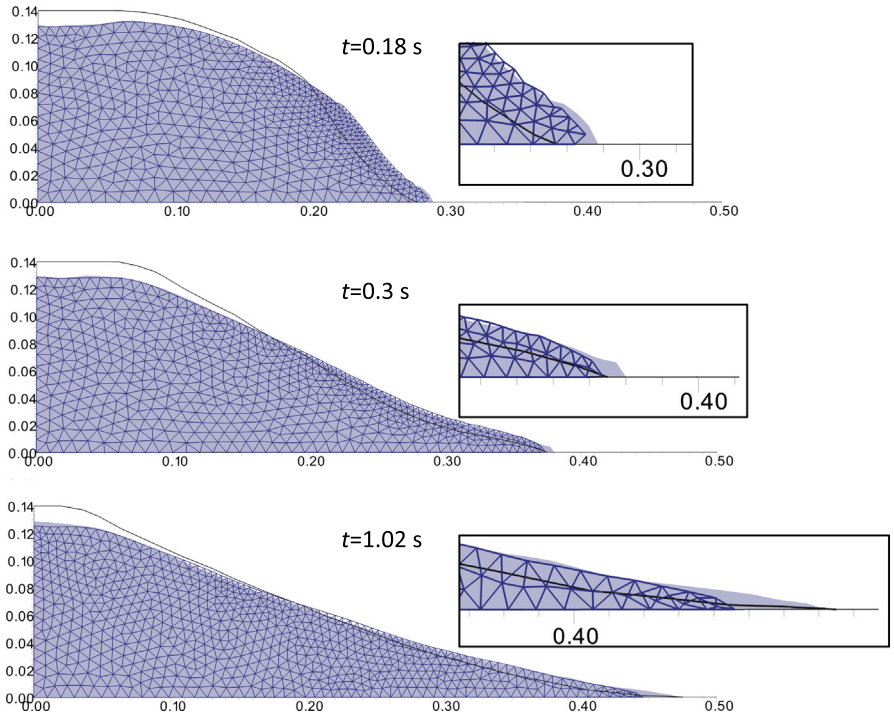

Fig. 6. Comparison between the simulations using variable viscosity $\eta(\|\boldsymbol{D}\|, p)$ (i.e. $\mu(I)$) (light gray) and constant viscosity with $\eta = 1$ Pa s (blue mesh) for granular column collapse at $\theta = 0^{\circ}$. The experimental results are represented by black lines. The inserts on the right are zooms near the front of the mass. (For interpretation of the references to color in this figure legend, the reader is referred to the web version of this article.)

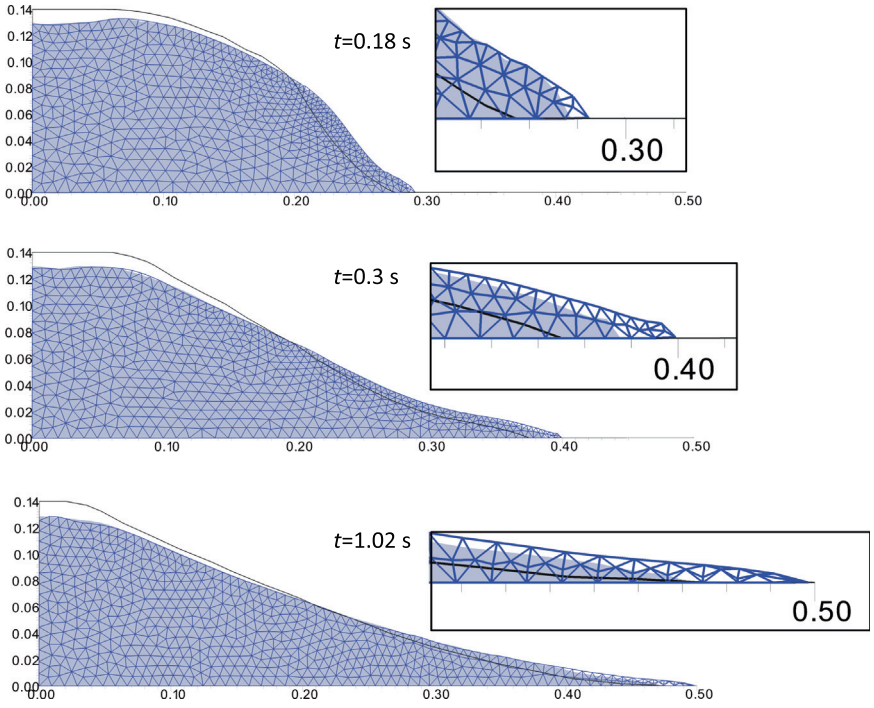

Fig. 7. Comparison between the simulations using variable viscosity $\eta(\|\boldsymbol{D}\|, p)$ (i.e. $\mu(I)$) (light gray) and constant viscosity with $\eta = 0.1$ Pa s (blue mesh) for granular column collapse at $\theta = 0^{\circ}$. The experimental results are represented by black lines. The inserts on the right are zooms near the front of the mass. (For interpretation of the references to color in this figure legend, the reader is referred to the web version of this article.)

of I lead to very high values of $\mu(I)$ at the free surface. However because μ is multiplied by p, these high values are compensated by a pressure of almost zero near the surface. The same is true in the vicinity of the front (Fig. 5). Within most of the flowing region, the friction coefficient is $0.5 < \mu(I) < 0.54$, corresponding to a friction angle between 26.5° and 28°. $\mu(I)$ increases significantly in the front zone with values higher than 0.6 in and just behind the front. The friction varies essentially from higher values near the bottom

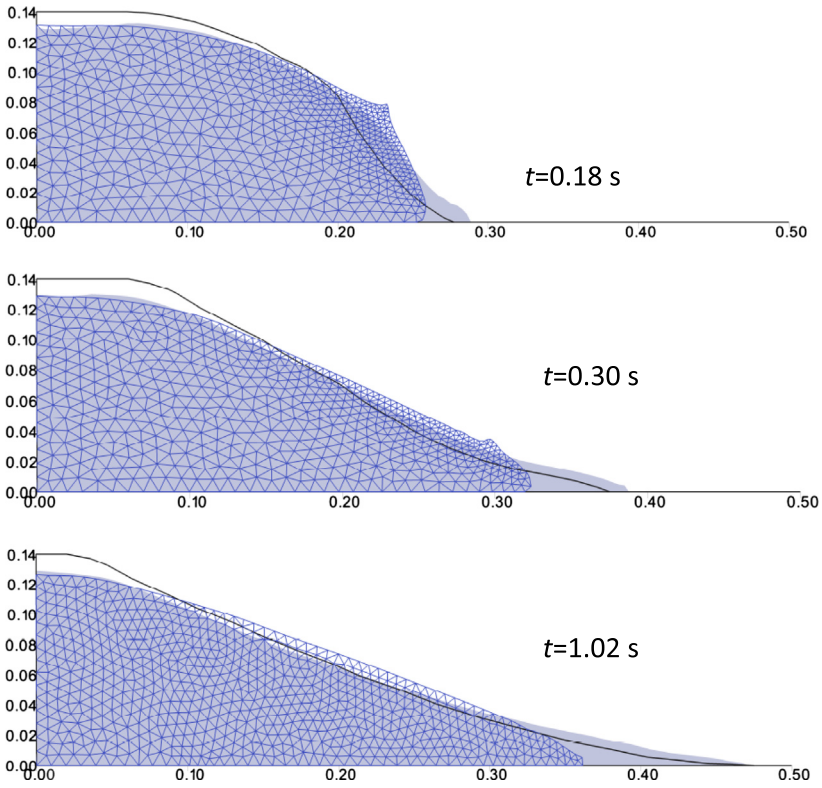

Fig. 8. Comparison between the simulations using variable viscosity $\eta(\|\boldsymbol{D}\|, p)$ (i.e. $\mu(I)$) (light gray) and constant viscosity with $\eta = 10$ Pa s (blue mesh) for granular column collapse at $\theta = 0^\circ$. The experimental results are represented by black lines. (For interpretation of the references to color in this figure legend, the reader is referred to the web version of this article.)

to lower values near the surface, except at the very top where the meaning of $\mu(I)$ is questionable as discussed above. This is different from the viscosity, which increases regularly frontwards within the flowing region.

For the constant viscosity rheology, we tested $\eta = 1$ Pa s, which is the order of magnitude of the 'real' viscosity derived from Eq. (14), a 10 times smaller viscosity $\eta = 0.1$ Pa s which is the minimum viscosity that we can handle with a reasonable computational time, and a 10 times larger viscosity $\eta = 10$ Pa s.

For the constant viscosity rheology, we tested $\eta = 1$ Pa s, which is the order of magnitude of the "real" viscosity derived from Eq. (14), along with a 10 times smaller viscosity $\eta = 0.1$ Pa s, which is the minimum viscosity that we can handle with a reasonable computational time, and a 10 times larger viscosity $\eta = 10$ Pa s.

Fig. 6 shows that very similar results are obtained when using a constant viscosity $\eta = 1$ Pa s and variable viscosity $\eta(\|\boldsymbol{D}\|, p)$. With this set of parameters, the mass flows slightly slower than with variable viscosity and the runout distance is slightly shorter (Fig. 6). While there is almost no difference between the simulations with the two rheologies at $t = 0.18$ s, the final runout distance is 5% shorter with $\eta = 1$ Pa s. This is because the variable viscosity is smaller than $\eta = 1$ Pa s in the flowing layer and near the front (Fig. 3)). With variable viscosity, a thinner front zone seems to develop at the very end of the mass ($t = 0.3$ s and $t = 1.02$ s in Fig. 6). Because the deposit is very thin near the front and several saltating beads were observed in the experiments, it is difficult to discriminate which law provides the best fit to the experimental results at the front [6,16]. The velocity distribution and the shape of the mass are very similar when using both constant ($\eta = 1$ Pa s) and variable viscosity. When using $\eta = 0.1$ Pa s, there are no major differences at times $t < 0.3$ s. However, at a later time, while the shape of the main mass is very similar (see Fig. 7), the front is thinner and is running faster. The final runout distance is about 5% longer than with variable viscosity, in agreement with Lagrée et al. 27]. Still the rest of the deposit behind the front has a very similar shape with $\eta = 0.1$ Pa s, $\eta = 1$ Pa s, and with variable viscosity. As a result, within this range of viscosities $0.1 < \eta < 1$ Pa s, the dissipation due to viscous effects is much smaller than that due to plastic deformation (i.e. strain-independent part of the "flowing constitutive relation"). For a higher though unrealistic viscosity ($\eta = 10$ Pa s), however, viscous effects strongly change the flow dynamics and deposit (see Fig. 8). Note that the computation is much faster when using constant viscosity $\eta = 1$ Pa s than when using variable viscosity which is in turn faster than when using $\eta = 0.1$ Pa s.

3.2. Collapse over an inclined plane $\theta = 16^\circ$

Up to now, simulations of granular collapse using a viscoplastic rheology have been performed only on a horizontal plane. Here we simulate the collapse over a moderate slope $\theta = 16^\circ$ using the same set of parameters. The results are qualitatively similar to those obtained on a horizontal plane. The simulation with variable viscosity reproduces the mass spreading relatively well (Fig. 9). The collapse of the mass at the upper end of the channel is however too fast in the simulations and the front also advances more rapidly than in the experiments. The shape of the final deposit is reproduced very well, except next to the back wall, where the computed maximum thickness is smaller, and at the front, where the thickness is slightly overestimated in the simulations. One possible explanation is that for $\theta = 16^\circ$, the flowing thickness (corresponding to the warmer colors in Fig. 9) is thicker than for $\theta = 0^\circ$ (Fig. 2). The maximum flowing thickness is about 0.1 m for $\theta = 16^\circ$ while it is about 0.05 m for $\theta = 0^\circ$. As a result, according to Taberlet et al.

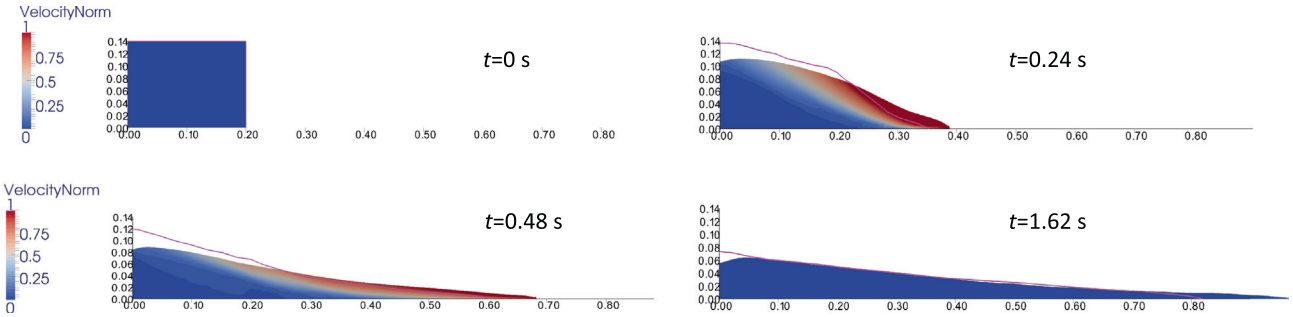

Fig. 9. Simulation using variable viscosity $\eta(\|\boldsymbol{D}\|, p)$ (i.e. $\mu(I)$): Comparison of the simulated granular mass and the experimental results (pink line) at different times for granular collapse over a plane inclined at $\theta = 16^\circ$. The colors represent the distribution of the norm of the computed velocity field $|\boldsymbol{u}|$ (in m/s). (For interpretation of the references to color in this figure legend, the reader is referred to the web version of this article.)

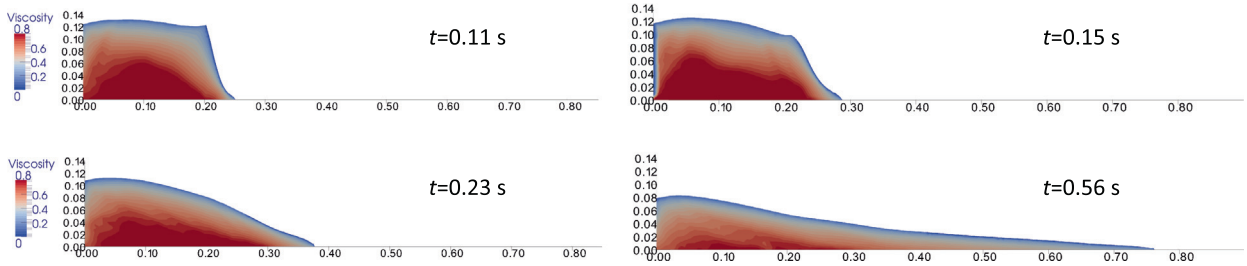

Fig. 10. Viscosity (in Pa s) calculated with the $\mu(I)$ rheology at different times for granular collapse over a plane inclined at $\theta = 16^\circ$.

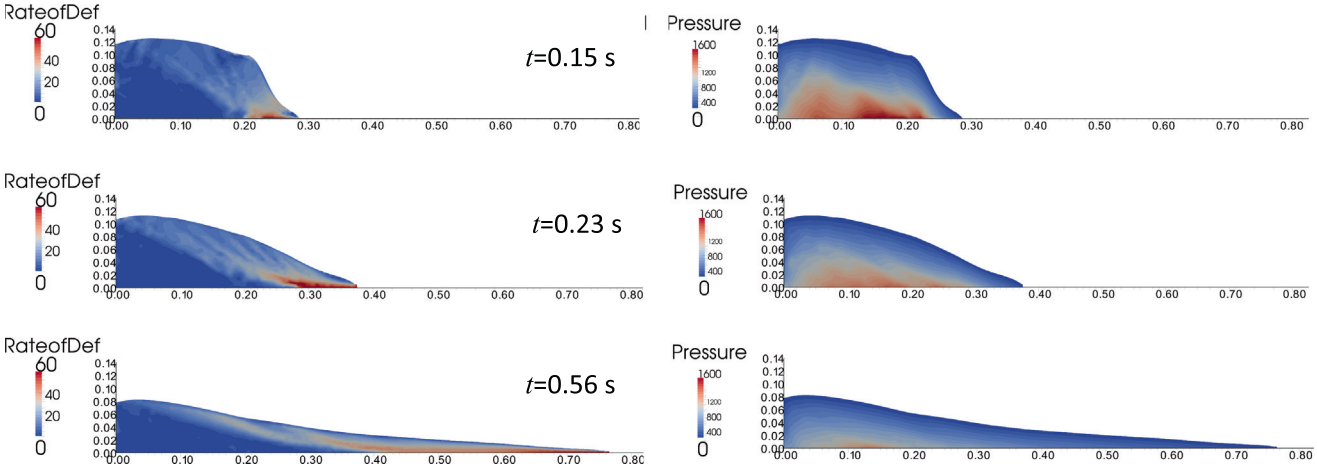

Fig. 11. Strain rate in s^{-1} (left column) and pressure in Pa (right column), calculated with variable viscosity $\eta(\|\boldsymbol{D}\|, p)$ (i.e. $\mu(I)$) at $t = 0.15$ s, $t = 0.23$ s, and $t = 0.56$ s for granular collapse over a plane inclined at $\theta = 16^\circ$.

[40] and Jop et al. [30], the effect of lateral wall friction should be two times greater in the experiments at $\theta = 16^\circ$ (see Section 2.2 for more details). This is not taken into account in our 2D simulations where the lateral wall friction and other friction coefficients are considered to be constant (i.e. not dependent on the flowing depth). Taking into account the real effect of the wall friction at $\theta = 16^\circ$ (3D simulations) would lead to shorter runout distances and to a smaller deposit thickness near the back wall, which would better match the experimental observations (see the next section).

The variable viscosity is slightly smaller near the static/flowing transition than at $\theta = 0^\circ$ but is almost the same within the flowing region where $0.1 < \eta < 0.7$ Pa s. The viscosity decreases towards the front where it is less than 0.5 Pa s. For example, at $t = 0.56$ s, the viscosity is lower than 0.3 Pa s over the 10 cm behind the front. In the flowing region, the viscosity gradually increases with the distance perpendicular to the free surface, seemingly mainly influenced by the increase in the pressure. Consequently, the viscosity mainly shows patterns similar to the pressure field (see Section 5), masking the influence of the strain rate. The strain rate distribution shows interesting features, with high strain rates concentrated initially near the bed close to the front and further upslope along most of the flowing region. The strain rate is distributed over almost the whole thickness of the flow near the front and over a significant thickness near the bed behind the front (Fig. 11 left column). The constant viscosity model leads to smaller front propagation velocities and therefore to shorter runout distances, in better agreement with experiments. At $t = 0.23$ s, periodic patterns develop in the strain rate distribution, possibly

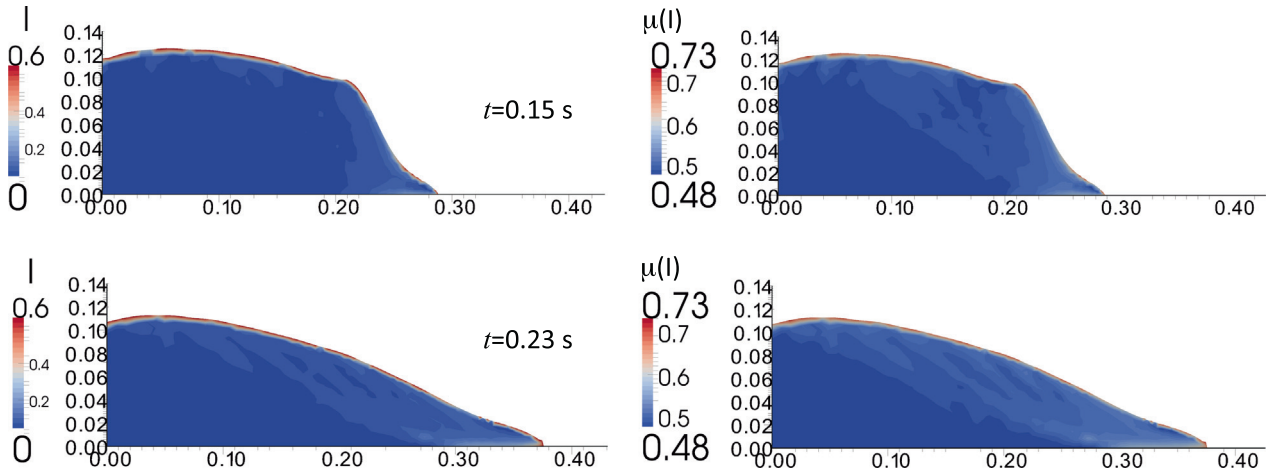

Fig. 12. Values of the inertial number I and of $\mu(I)$ calculated in the model with the $\mu(I)$ rheology at different times for granular collapse over a plane inclined at $\theta = 16^{\circ}$.

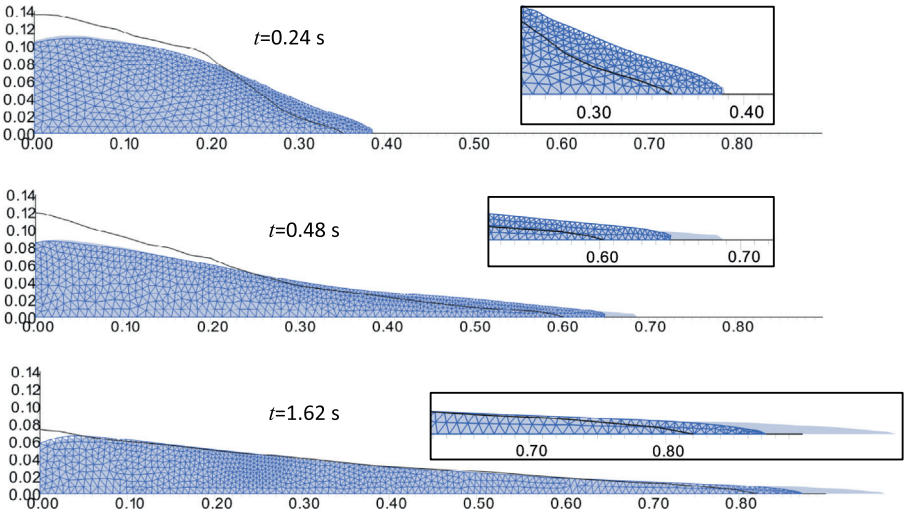

Fig. 13. Comparison between the simulations using variable viscosity $\eta(\|\boldsymbol{D}\|, p)$ (i.e. $\mu(I)$) (light gray) and constant viscosity with $\eta = 1$ Pa s (blue mesh) at different times for granular collapse over a plane inclined at $\theta = 16^{\circ}$. The experimental results are represented by black lines. The inserts on the right correspond to zooms near the front of the mass. (For interpretation of the references to color in this figure legend, the reader is referred to the web version of this article.)

related to flow instabilities (see Section 5). Similar patterns are observed for I and $\mu(I)$ (Fig. 12).

Fig. 13 shows again that the results are very similar for constant ($\eta = 1$ Pa s) and variable viscosity rheologies. For the constant viscosity, the mass spreads slower and the runout distance is shorter, in better agreement with experimental results.

4. Influence of the boundary conditions

Note that, given the very similar results obtained with variable $\eta(\|\boldsymbol{D}\|, p)$ and constant viscosity ($\eta = 1$ Pa s) and given the shorter computational time required for constant viscosity, we will use a constant viscosity of $\eta = 1$ Pa s in all the following simulations.

4.1. Influence of the gate

Gate removal at the start of the avalanche has always been thought to have negligible influence on granular collapse dynamics and deposits. To check this, we considered two scenarios: in the first, the mass is released instantly (no gate) and in the second, the granular mass is in frictionless contact with a gate that is removed at a speed of $V_b = 2.3\ \mathrm{m\,s^{-1}}$ in the direction perpendicular to the inclined bed.

In the scenario with the gate, the flow initiates near the bottom of the granular column (dark blue in Fig. 14), while in the scenario with no gate (light blue mesh), the mass spreads from the top of the granular mass. As expected, at the beginning of the flow the scenario with the gate is much closer to the experimental data represented in pink lines.

The initial rise at the top front edge of the released mass in the experiments ($t = 0.06$ s in Figs. 14 and 15) is not reproduced in the simulations. This is because in the simulations, there is a frictionless contact between the mass and the gate, while in reality friction occurs at the contact.

During all the spreading, in the scenario with the gate, the front advances less rapidly and the thickness of the mass is generally smaller near the front than when the gate is not taken into account. At a later time (e.g. $t = 0.3$ s in Fig. 14), the thickness of the mass in the upper part of the channel is the same, but the front is still further upstream.

We show here that the scenario with the gate better fits the dynamics of the experimental collapse. Interestingly, the final deposit is however the same for both two scenarios: the gate has

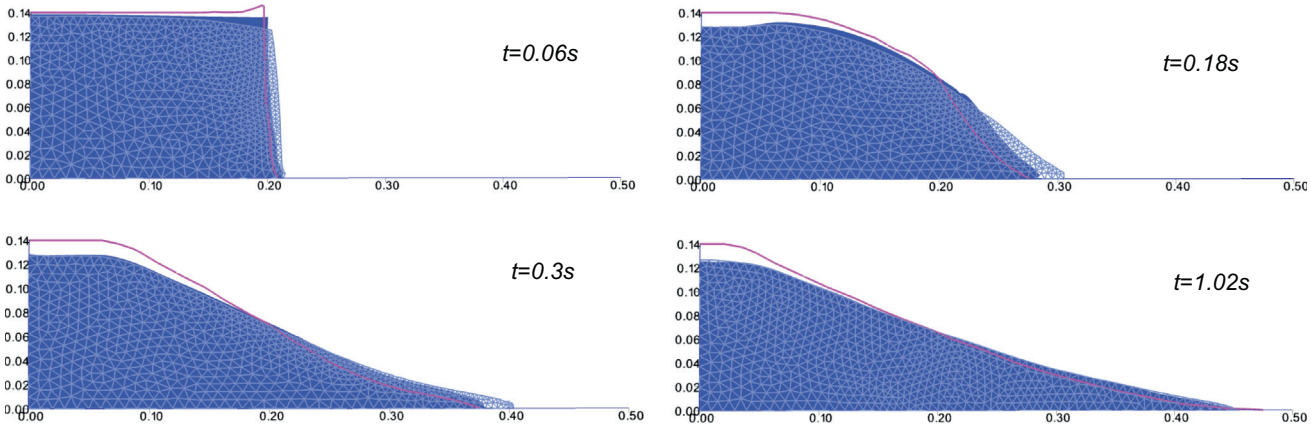

Fig. 14. Influence of the gate on granular collapse over a horizontal plane $\theta = 0^\circ$. Comparison of the thickness of the granular mass simulated with the gate (light blue) and without the gate (blue mesh), as well as the experimental results (pink line) at different times. (For interpretation of the references to color in this figure legend, the reader is referred to the web version of this article.)

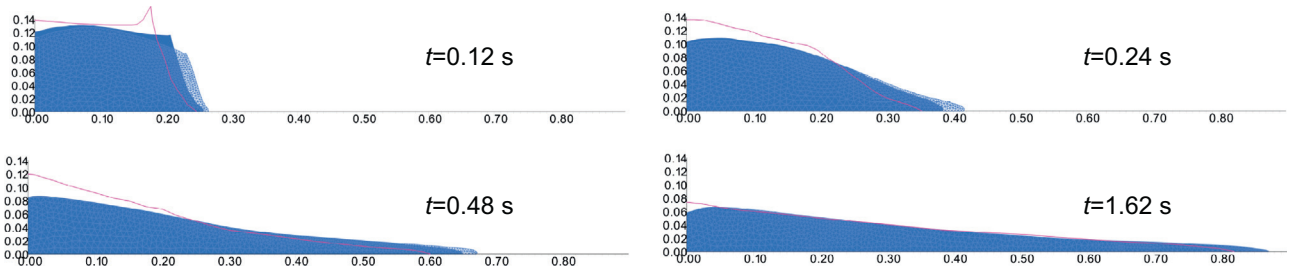

Fig. 15. Influence of the gate on granular collapse over an inclined bed $\theta = 16^\circ$. Comparison of the thickness of the granular mass simulated with the gate (light blue) and without the gate (blue mesh), as well as the experimental results (pink line) at different times. (For interpretation of the references to color in this figure legend, the reader is referred to the web version of this article.)

an influence on the flow dynamics that disappears in the deposition phase. The same qualitative behavior is observed for granular collapses over inclined beds (Fig. 15). The influence of the gate is even greater at $\theta = 16^\circ$ than at $\theta = 0^\circ$. These results are in good agreement with the simulations of Carbopol flows over a horizontal plane performed by Martin Rentschler [44]. The influence of the gate may explain why Lacaze et al. [14] obtained a faster front propagation in their discrete element simulations than in their experiments while reproducing the experimental runout distance, even though their way of removing the gate was different (see their Fig. 4). However, for a very slow gate removal the runout distance is significantly shorter (see Meriaux [45]).

4.2. Influence of friction on the back wall and at the bed

Increasing the friction on the back wall from $\mu_w = \tan 10.5^\circ$ to $\mu_w = \tan 25.5^\circ$ in the simulations has only a very slight influence on the flow. In particular, it does not improve the overestimation of the collapse of the granular mass near the back wall. As already discussed above, the pressure near the upper half of the back wall is small and therefore the friction force is always small whatever the friction coefficient at the wall. Near the bottom of the back wall, the pressure is higher but their is no motion. In the experiments, the presence of lateral walls may significantly change this picture. For instance, the presence of the lateral walls may increase the pressure in their vicinity, which may increase the friction force near the back wall and thus reduce the vertical collapse of the mass in its vicinity.

Our simulations indicate that part of the mass slides at the bed near the front for a basal friction coefficient $\mu_b = 0.48$ (see Figs. 2 and 8), contrary to what was assumed in other simulations where a no-slip condition (i.e. adherence) was imposed at the bottom (e.g. Lagrée et al. [27], Crosta et al. [17]). To investigate the influence of the basal boundary condition, we imposed either real adherence (zero velocity) or a very high friction coefficient at the bed. Imposing adherence reduces the collapse of the mass near the back wall leading to a maximum thickness of the deposit h_f about 4% higher than with the a basal friction coefficient $\mu_b = 0.48$ (see Fig. 16). It also reduces the runout distance by 10%. As a result, the simulation with adherence better fits the results near the back wall but underestimates the runout distance. If, instead of imposing adherence, we impose a very high friction coefficient at the bottom ($\mu_b = 4.8$), we obtain a maximum thickness near the back wall and a runout distance that are in between the simulation with adherence and that with a basal friction coefficient of μ_b (Fig. 17). In fact, the normal stress near the front is very small and even with a very high friction coefficient, the friction force is still small enough to produce a difference between this dissipative force and the driving forces that allows the material to slip on the basal surface. As a result, sliding at the bed is allowed near the front, contrary to the case of adherence. Note that in Lagrée et al. [27], the mass spreads less rapidly in their continuum simulation than in their DEM simulations. One explanation could be that in their continuum model, they imposed no-slip boundary conditions while there is a significant slip velocity near the front.

5. Insight into the flow dynamics

5.1. Velocity distribution

Fig. 18 shows the distribution of the horizontal velocity at $\theta = 0^\circ$ as well as its vertical profiles at some fixed locations along

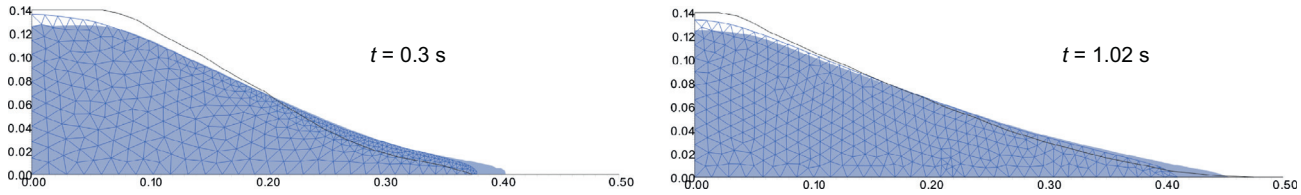

Fig. 16. Influence of the boundary conditions at the bed on granular collapse over a horizontal plane $\theta = 0^{\circ}$. Comparison of the thickness of the granular mass simulated in the "no gate" scenario with friction (dark blue) and with adherence (light blue mesh), as well as the experimental results (black lines) at different times. (For interpretation of the references to color in this figure legend, the reader is referred to the web version of this article.)

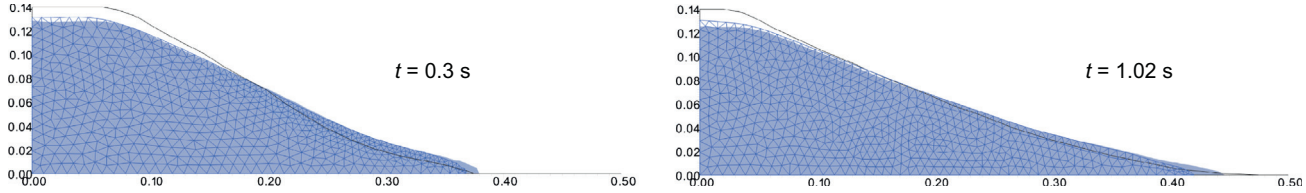

Fig. 17. Influence of the boundary conditions at the bed on granular collapse over a horizontal plane $\theta = 0^{\circ}$. Comparison of the thickness of the granular mass simulated in the "gate" scenario with friction (light blue) and with high friction (blue mesh), as well as the experimental results (black line) at different times. (For interpretation of the references to color in this figure legend, the reader is referred to the web version of this article.)

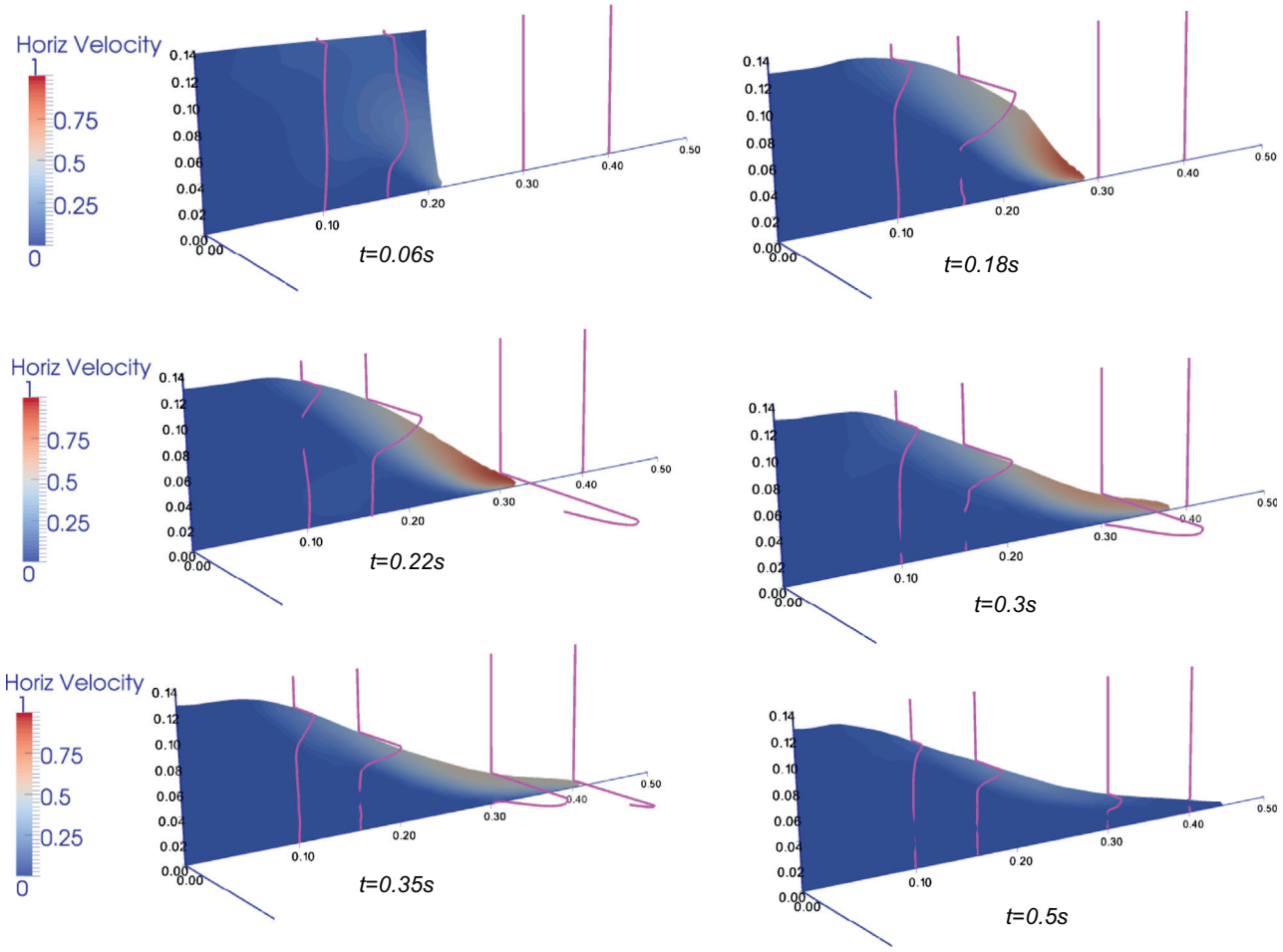

Fig. 18. The distributions of the horizontal velocity u_x (color scale in m/s) and vertical profiles (pink lines) of the horizontal velocity $u_x(z)$ at four fixed locations $x = 10$, 15, 30 and 40 cm along the channel, from simulations with the Drucker–Prager model with constant viscosity $\eta = 1$ Pa s over the horizontal plane $\theta = 0^{\circ}$. Note that the vertical profiles are represented in the plane perpendicular to the simulated flow. (For interpretation of the references to color in this figure legend, the reader is referred to the web version of this article.)

the channel (at $x = 10, 15, 30$ and 40 cm) (pink lines). In the first snapshot, at $t = 0.06$ s, just after the gate was lifted, the maximum horizontal velocity is reached close to the bed. This is the result of gate removal, which induces a flow starting near to the bottom. Later, the flow is concentrated only in a shallow sub-domain near the free surface as observed with the norm of the velocity field. The maximum horizontal velocity is reached near the free surface. In the flowing region, the horizontal velocity has a parabolic profile with an exponential decay near the flow/no-flow transition. Near the front, the granular mass slips at the contact with the bed surface, i.e. the basal velocity is not equal to zero (for example at $t = 0.22$ s and $x = 30$ cm or at $t = 0.35$ s and $x = 40$ cm). Fig. 18 suggests that the horizontal velocity can change direction (i.e. negative horizontal velocity) in the quasi-static region (e.g. at $t = 0.18, 0.22, 0.3$ s). However these negative velocities are small and close to the expected numerical error.

The maximum downward and upward vertical velocities are about 0.6 m s^{-1} and 0.06 m s^{-1}, respectively (Fig. 19). As a result, the downward vertical velocity can be as high as half the horizontal velocity. Fig. 19 clearly shows, at $t = 0.18$ s, an interface between a zone with no vertical velocity and a zone with a small downward velocity. Under this rough interface, a localized zone of upward velocity develops (dark red color and negative vertical velocity in Fig. 19 at $t = 0.18, 0.3$ s). Within the small vertical velocity regions underlying the main flowing layer (red colors), the vertical velocity distribution is not regular and exhibits spatio-temporal fluctuations at a scale of a few centimeters or more.

5.2. Yield limit distribution and stagnant zones

The yield limit $\kappa = \mu_s p$, which has the same distribution as the pressure p (plotted in Fig. 4 (right)), has an almost gravitational distribution. The distribution of the stress deviator $\|\boldsymbol{\sigma}'\|$, plotted in Fig. 20 (right), is rather different. The maximum value is reached around mid-depth in the granular material and decreases rapidly near the free surface and towards the bed at the back wall. Note that, except near the bed at the back wall, the yield stress and stress deviator have the same order of magnitude (i.e. the same color on the color scale), which means that the yielding surface separating flow and no-flow zones could change significantly during the experiment. For $t = 0.3$ s and $t = 0.42$ s, the yield limit (pressure) distribution presents an unexpected zone of weakness (low pressure). This (non-static) sucking zone, which is localized on a sloping line, appears before the granular mass reaches a configuration close to equilibrium and is associated with a slightly positive vertical velocity.

The static/flowing transition can be seen in the left side of Fig. 20, where we have plotted the distribution of the yield function $F(\boldsymbol{\sigma}) := \|\boldsymbol{\sigma}'\| - \mu_s p$. The zone corresponding to a positive yield function (dark red) represents the flowing region of the granular mass, while the evolution of the strain rate is plotted in Fig. 4 (left). Note that for $t = 0.18$ s and $t = 0.30$ s, the regions with a high strain rate are located near the tip of the granular mass, near the bed surface. In these regions, the inertial and gravitational forces are opposed by the frictional forces, producing a high shear in the granular mass. As we can see by comparison with Fig. 20 (right), these high deformation regions are not related to high stress deviator zones. This confirms the nonlinear character of the constitutive law (7). Furthermore, Fig. 4 (left) shows the development of shear bands during the beginning of the spreading.

For $t = 0.3$ s and $t = 0.42$ s, the yielding surface is not clearly determined. Indeed, we remark that behind the main flowing region (in front of the granular mass near the free surface) there are some zones corresponding to a non-vanishing strain rate in Fig. 4 (left). These small regions are related to the "weakness zones" of low yield limit (or pressure) described above. Note that for all the computations presented above, we did not use any special techniques for tracking the yield surface. A more detailed investigation of the static/flowing transition could be carried out using the re-meshing techniques developed for stationary flows (see for instance [46,47]) at each time step. This would however imply a major increase in computational effort.

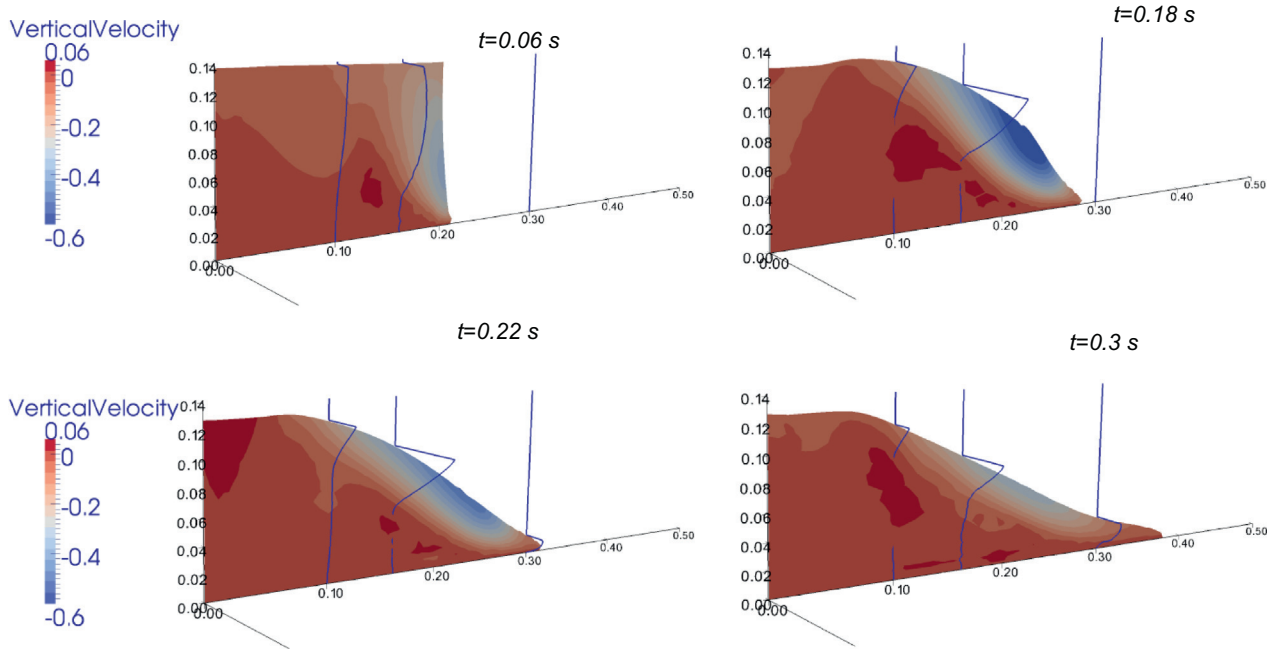

Fig. 19. The distribution of the vertical velocity u_y (color scale in m/s) and vertical profiles (blue lines) of the vertical velocity $u_y(z)$ at three fixed locations $x = 10$, 15 and 30 cm along the channel, from simulations with the Drucker–Prager model with constant viscosity $\eta = 1$ Pa s over the horizontal plane $\theta = 0°$. Note that the vertical profiles are represented in the plane perpendicular to the simulated flow. (For interpretation of the references to color in this figure legend, the reader is referred to the web version of this article.)

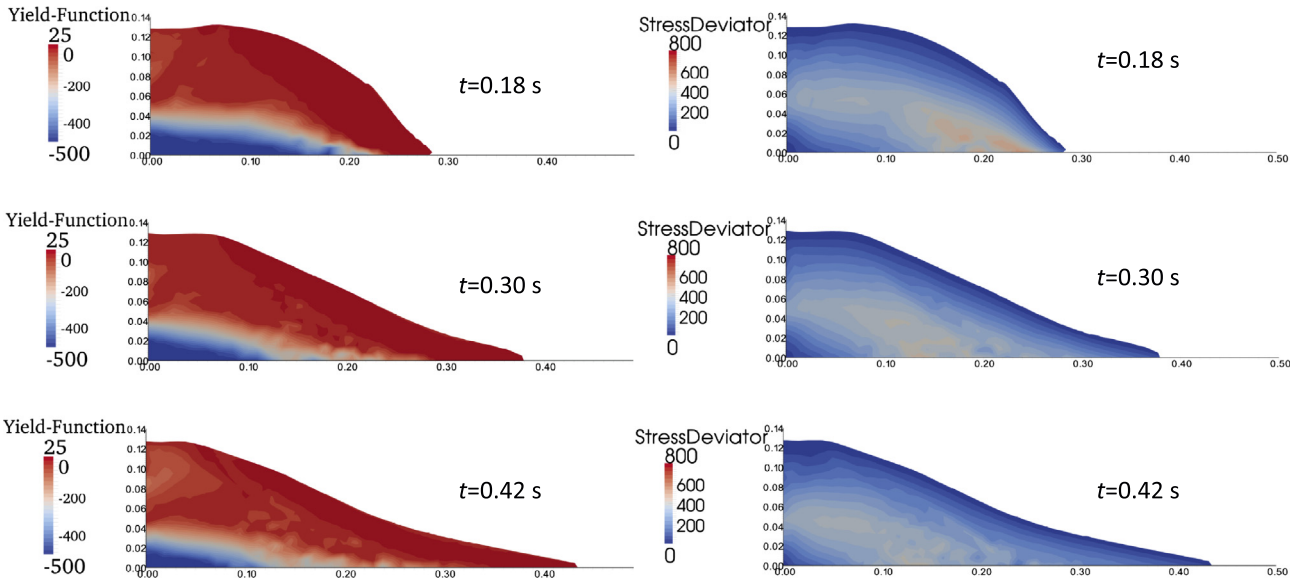

Fig. 20. The distribution of the yield function $F(\boldsymbol{\sigma}) := \|\boldsymbol{\sigma}'\| - \kappa$ (left, color scale in Pa) and of the stress deviator $\|\boldsymbol{\sigma}'\|$ (right) in the granular mass $\mathcal{D}(t)$ for different times (color scale in Pa). (For interpretation of the references to color in this figure legend, the reader is referred to the web version of this article.)

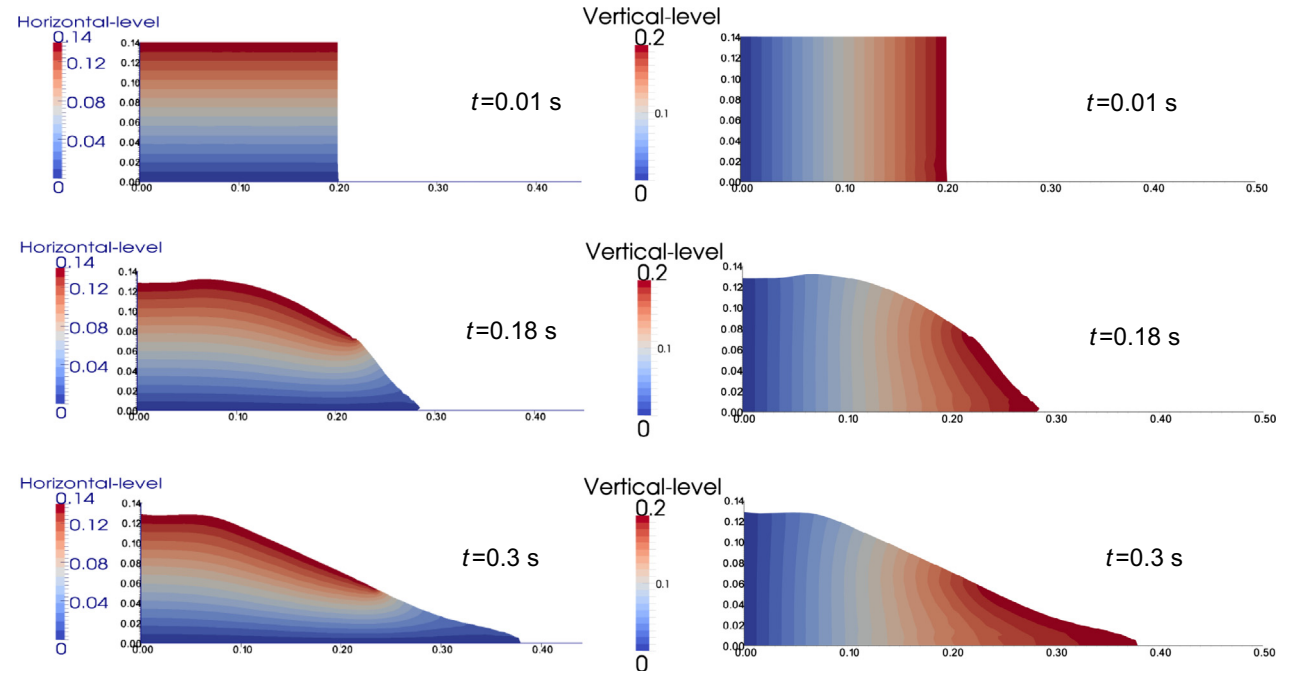

Fig. 21. Deformation of the initially horizontal layers (left) and initially vertical layers (right) calculated for granular collapse on a horizontal plane $\theta = 0^\circ$ (color scale in m). (For interpretation of the references to color in this figure legend, the reader is referred to the web version of this article.)

5.3. Deformation of horizontal and vertical layers

Fig. 21 shows how artificial initially horizontal and vertical layers deform during the flow. At time $t = 0.18$ s, the top horizontal layers near the back wall are collapsing vertically more rapidly than between $x = 0.05$ and 0.1 m. Further towards the front, the top layers become thinner and appear to converge toward a stamp point at the surface, corresponding to the advancing top front edge of the initial column. Under and next to this point, the horizontal layers bend, first downwards while thinning and then upwards while thickening towards the front. Interestingly, the deposit in the first two thirds of the channel is made of the same succession of layers as the initial mass, even though these layers are deformed. On the other hand, in the final third of the channel, the deposit behind the front is made of the layers initially located below mid-depth of the initial column. This may be different for columns with high aspect ratios (see Thomson and Huppert [48]). This observation may be important in the interpretation of real deposits. The deformation of the artificial initially vertical layers is very similar to that obtained by Lagrée et al. [27] using the $\mu(I)$ rheology (see their Fig. 9), except near the bed where the boundary conditions are different (sliding friction here and no-slip

in their simulations). As a result, the deformations of the inner vertical layers are not specifically related to the $\mu(I)$ rheology.

6. Discussion and conclusion

We propose a mechanical and numerical model for granular flows based on Drucker–Prager plasticity (pressure-dependent yield stress) with either a constant viscosity or a variable viscosity $\eta(\|\boldsymbol{D}\|, p)$ depending on both the pressure p and the norm of the strain rate tensor $\|\boldsymbol{D}\|$, based on the reformulation of the so-called $\mu(I)$ rheology.

We have shown here that the Drucker–Prager plasticity criterion and a variable or constant viscosity reproduce quantitatively the dynamics and deposits of the granular collapse of columns with small aspect ratios (here $a = 0.7$) over horizontal and inclined planes, using rheological parameters derived from experiments, without any fitting procedure. Note that we have taken into account the initial removal of the gate that releases the granular column. The Drucker–Prager rheology with constant viscosity ($\eta = 1$ Pa s) and variable viscosity $\eta(\|\boldsymbol{D}\|, p)$ (i.e. the $\mu(I)$ rheology) provide very similar results. The numerical simulation shows that the main differences are located near the front. Indeed, the parameter I of the $\mu(I)$ rheology varies mainly in this region. Interestingly, the region near the front is characterized by thin flows over a rigid bed, a situation close to that for which the $\mu(I)$ rheology was established. While variable-viscosity $\eta(\|\boldsymbol{D}\|, p)$ rheology may be crucial to simulate different regimes such as the collapse of high aspect ratio columns [27], the strong similarity of the two rheologies in the case studied here is an important result in terms of application to natural landslides that have typical aspect ratios lower than 1 (see Lucas et al. [49] for a compilation of real data). An intermediate linearized approach (23) and (24) can also be used. Indeed, for the Drucker–Prager rheology with constant viscosity, only two rheological parameters are needed, compared to three for variable viscosity (and two for the linearized law). Furthermore, calculations with a constant viscosity of $\eta = 1$ Pa s requires much less computational time (at least for the numerical approach presented here). A crucial contribution of the expression of the viscosity $\eta(\|\boldsymbol{D}\|, p)$ (Eq. (14)) derived from the $\mu(I)$ rheology is to provide the order of magnitude of the viscosity in a specific situation without performing simulations. For example, Eq. (14) gives a constant value of viscosity ($\eta = 1$ Pa s here) that makes it possible to reproduce the experimental results, while numerical simulations show that the variable viscosity ranges from values up to $\eta = 1.5$ Pa s in the deep quasi-static regions down to zero near the free surface. Discriminating constant and variable viscosity rheologies in the regimes of granular collapse of small aspect ratio columns on inclined beds would necessitate more a detailed comparison with measured velocity profiles.

The gate has a significant impact on the flow dynamics but the deposits obtained with and without the gate are almost the same. The deposit seems thus to depend only on the initial energy of the column and on the mean dissipative forces at work during the flow, provided gate removal is not too slow [45].

As the slope of the bed increases, these models slightly overestimate the flow velocity and runout distance. This may be due to lateral wall friction that increases with increasing thickness of the flowing layer at higher slopes. This effect is not accounted for in the 2D simulations. As in discrete element modeling, 3D viscoplastic modeling of the wall effect will certainly increase the dissipation due to the wall as the slope increases but will also increase the pressure, in particular near the wall at the back of the reservoir, thus increasing the friction in this region. This will certainly reduce the overestimated collapse of the columns near the back wall. On the other hand, simulations show that there is significant sliding of the mass on the bed near the front. As a result, imposing adherence near the bed, as in previous studies, would seem to be inappropriate. To confirm this, we investigated the influence of the friction on the back wall and at the bed. For the bed, we imposed either real adherence (zero-velocity) or a very high friction coefficient. Imposing adherence at the bed reduces the collapse of the mass near the back wall but also reduces the runout distance by 10%. As a result, the simulation with adherence better fits the results near the back wall but underestimates the runout distance. By choosing a very high friction coefficient at the bed, sliding is allowed near the front and the computed runout distance is in between the simulation with adherence and that with normal friction. Note that the normal stress is very small near the front and therefore even with a very high friction coefficient, the friction force is still small enough to produce a difference between this dissipative force and the driving forces that allows basal sliding.

Except at the very start during the gate removal period, the yield limit has an almost gravitational distribution while the stress deviator reaches its maximum value at mid-flow height. The "constitutive" flowing region (i.e. with a positive yield function) near the free surface is globally well delimited and corresponds to a non-vanishing velocity zone and a non-vanishing strain rate zone. However, during the flow, the yield limit distribution presents a zone of weakness (low pressure), localized on a sloping line and associated with a slightly positive vertical velocity.

The regions with high strain rates are located behind the front tip of the granular mass, near the bed, where high shear of the granular mass is expected as a result of the action of the driving (inertial and gravitational) forces and the frictional forces. These high deformation regions are not related to high stress deviator zones, confirming the strong nonlinear character of the viscoplastic law. Furthermore, the development of shear bands during the beginning of the spreading on an inclined plane is observed. The coherent blocks of material observed on the upslope deposits of some large landslides could be the result of such shear bands [60].

The numerical simulation of the 2D collapse of granular columns shows that the flow involves only a shallow layer of granular material. Despite the heterogeneities observed within the flow, especially near the static/flowing transition, the velocity profiles essentially exhibit a typical shape with a maximum velocity at the free surface, a Bagnold-like to linear profile and an exponential decrease of the velocity near the static/flowing transition. The pressure seems to be close to hydrostatic in this flowing region. These results provide new constraints for developing thin layer models with a flowing layer overtopping a static zone (see e.g. Bouchut et al. [50,51]).

Acknowledgements

The authors are thankful to Yoël Forterre, Christophe Ancey, Guillaume Ovarlez, John de Bruyn and Maxime Farin for fruitful discussions. This work has been partially funded by the ANR contract ANR-11-BS01-0016 LANDQUAKES, CNCS-UEFISCDI project PN-II-ID-PCE-2011-3-0045, the USPC PAGES project, and the ERC contract ERC-CG-2013-PE10-617472 SLIDEQUAKES.

Appendix A. Numerical method

We propose here a numerical algorithm to solve the dynamic flow problem described above. We use a time implicit (backward) Euler scheme for the time discretization of the field equations, which gives a set of nonlinear equations for the velocity $\boldsymbol{u}$, the deviatoric stress tensor $\boldsymbol{\sigma}'$ and the pressure p. At each iteration in time, an iterative algorithm is used to solve these nonlinear

equations. Note that in the case of the proposed viscoplastic model, numerical difficulties arise from the non-differentiability of the viscoplastic and friction terms. This means that the numerical techniques developed for Navier–Stokes fluids cannot be used. To overcome these difficulties, the iterative decomposition–coordination formulation coupled with the augmented Lagrangian method of [52,53] is adapted here.

To include frictional effects in the algorithm, we first regularize the friction law (20). This can be done (see also [33,54]) by introducing a small frictional viscosity $\eta_f \ll 1$ in the Coulomb friction law and writing (20) as

$$\boldsymbol{u}_T = -\frac{1}{\eta_f}\left[1-\frac{\mu_C[-\sigma_n]_+}{|\,\boldsymbol{\sigma}_T\,|}\right]_+\boldsymbol{\sigma}_T, \tag{25}$$

where, as before, $[\,]_+$ is the positive part. Note that using this regularization, the friction law has the same mathematical structure as the viscoplastic constitutive Eq. (8) and we can use the same iterative decomposition–coordination formulation. For all the computations for the present paper, the regularization frictional viscosity coefficient was chosen to be $\eta_f = 0.1$ Pa s m^{-1}.

An ALE (Arbitrary Lagrangian–Eulerian) description is used to compute the evolution of the fluid domain $\mathcal{D}$. For the sake of simplicity, we will not present here the ALE formulation of the numerical scheme. As a matter of fact, the numerical algorithm proposed here deals only with a Stokes-type problem at each time step and the implementation of the Navier–Stokes equations in an ALE formulation is rather standard (see for instance [55–58]).

A.1. Time discretization

Let Δt be the time step and $\boldsymbol{u}^k$, $\boldsymbol{\sigma}'^k$ and p^k be the values of the unknowns $\boldsymbol{u}(k\Delta t), \boldsymbol{\sigma}'(k\Delta t)$ and $p(k\Delta t)$. Let us also assume that we have computed all these variables at time $t = (k-1)\Delta t$.

The time implicit (backward) Euler scheme for the field Eqs. (15), (16) and (8) gives the following nonlinear equations for the unknowns $\boldsymbol{u}^k, \boldsymbol{\sigma}'^k$ and p^k

$$\rho\left(\frac{\boldsymbol{u}^k-\boldsymbol{u}^{k-1}}{\Delta t}+\boldsymbol{u}^k\cdot\nabla\boldsymbol{u}^k\right)-\mathbf{div}\,\boldsymbol{\sigma}'^k+\nabla p^k=\rho\boldsymbol{f}\quad\text{in}\quad\mathcal{D}, \tag{26}$$

$$\mathrm{div}(\boldsymbol{u}^k)=0\quad\text{in}\quad\mathcal{D}, \tag{27}$$

$$\boldsymbol{D}(\boldsymbol{u}^k)=\frac{1}{2\eta(\|\boldsymbol{D}(\boldsymbol{u}^k)\|,p^k)}\left[1-\frac{\kappa(p^k)}{\|\boldsymbol{\sigma}'^k\|}\right]_+\boldsymbol{\sigma}'^k, \tag{28}$$

while the boundary conditions read

$$\boldsymbol{\sigma}^k\boldsymbol{n}=0\quad\text{on}\quad\Gamma_s, \tag{29}$$

$$\boldsymbol{u}^k\cdot\boldsymbol{n}=0,\quad \boldsymbol{u}_T^k=-\frac{1}{\eta_f}\left[1-\frac{\mu_C[-\sigma_n^k]_+}{|\,\boldsymbol{\sigma}_T^k\,|}\right]_+\boldsymbol{\sigma}_T^k,\quad\text{on}\quad\Gamma_b. \tag{30}$$

A.2. The algorithm at each time step

Let us fix the iteration in time, k. In order to describe the algorithm, let $r, r_f > 0$ be the augmented Lagrangian coefficients. We start with $\boldsymbol{u}^{k,0}=\boldsymbol{u}^{k-1}, \boldsymbol{\sigma}'^{k,0}=\boldsymbol{\sigma}'^{k-1}, \boldsymbol{\sigma}_T^{k,0}=\boldsymbol{\sigma}_T^{k-1}$ and let $\boldsymbol{u}^{k,n-1}, \boldsymbol{\sigma}'^{k,n-1}$ and $\boldsymbol{\sigma}_T^{k,n-1}$ be known. We also assume that the strain rate multipliers $\dot{\boldsymbol{\gamma}}^{k,n-1}:\mathcal{D}\to\mathbb{R}^{3\times3}_S$ and slip rate multipliers $\delta^{k,n-1}:\Gamma_b\to\mathbb{R}^2$ introduced below are known. Convergence is achieved when the difference between $\boldsymbol{u}^{k,n}, \boldsymbol{\sigma}'^{k,n}, p^{k,n}, \boldsymbol{\sigma}_T^{k,n}$ and $\boldsymbol{u}^{k,n-1}, \boldsymbol{\sigma}'^{k,n-1}, p^{k,n-1}, \boldsymbol{\sigma}_T^{k,n-1}$ is sufficiently small.

Step 1. The first step consists in solving the following linear equation of the Stokes type for the velocity field $\boldsymbol{u}^{k,n}$ and the pressure $p^{k,n}$:

$$\mathrm{div}(\boldsymbol{u}^{k,n})=0, \tag{31}$$

$$\rho\left(\frac{\boldsymbol{u}^{k,n}-\boldsymbol{u}^{k-1}}{\Delta t}+\boldsymbol{u}^{k,n-1}\cdot\nabla\boldsymbol{u}^{k,n}\right)-\mathbf{div}\big(r\boldsymbol{D}(\boldsymbol{u}^{k,n})\big)+\nabla p^{k,n}$$
$$=\mathbf{div}\big(\boldsymbol{\sigma}'^{k,n-1}-r\dot{\boldsymbol{\gamma}}^{k,n-1}\big)+\rho\boldsymbol{f}, \tag{32}$$

with the boundary conditions

$$\big(r\boldsymbol{D}(\boldsymbol{u}^{k,n})-p^{k,n}\boldsymbol{I}+\boldsymbol{\sigma}'^{k,n-1}-r\dot{\boldsymbol{\gamma}}^{k,n-1}\big)\boldsymbol{n}=0,\quad\text{on}\quad\Gamma_s,$$

$$\boldsymbol{u}^{k,n}\cdot\boldsymbol{n}=0,\quad\text{on}\quad\Gamma_b,$$

$$\big(r\boldsymbol{D}(\boldsymbol{u}^{k,n})-p^{k,n}\boldsymbol{I}+\boldsymbol{\sigma}'^{k,n-1}-r\dot{\boldsymbol{\gamma}}^{k,n-1}\big)_T$$
$$=-r_f\boldsymbol{u}_T^{k,n}+r_f\delta^{k,n-1}+\boldsymbol{\sigma}_T^{k,n-1},\quad\text{on}\quad\Gamma_b.$$

Step 2. First we update the viscosity coefficient $\eta=\eta(\|\boldsymbol{D}(\boldsymbol{u}^{k,n})\|,p^{k,n})$ and the yield limit $\kappa=\kappa(p^{k,n})$. Then, we compute the strain rate multipliers $\dot{\boldsymbol{\gamma}}^{k,n}$ and the slip rate multipliers $\delta^{k,n}$

$$\dot{\boldsymbol{\gamma}}^{k,n}=\frac{1}{2\eta+r}\left[1-\frac{\kappa}{\|\boldsymbol{\sigma}'^{k,n-1}+r\boldsymbol{D}(\boldsymbol{u}^{k,n})\|}\right]_+(\boldsymbol{\sigma}'^{k,n-1}+r\boldsymbol{D}(\boldsymbol{u}^{k,n})), \tag{33}$$

$$\delta^{k,n}=-\frac{1}{\eta_f+r_f}\left[1-\frac{\mu_C[-\sigma_n^{k,n-1}]_+}{|\,\boldsymbol{\sigma}_T^{k,n-1}-r_f\boldsymbol{u}_T^{k,n}\,|}\right]_+(\boldsymbol{\sigma}_T^{k,n-1}-r_f\boldsymbol{u}_T^{k,n}), \tag{34}$$

according to the decomposition–coordination formulation coupled with the augmented Lagrangian method.

Step 3. Finally, we update the stress deviator $\boldsymbol{\sigma}'^{k,n}$ and the tangential stress $\boldsymbol{\sigma}_T^{k,n}$ using

$$\boldsymbol{\sigma}'^{k,n}=\boldsymbol{\sigma}'^{k,n-1}+r(\boldsymbol{D}(\boldsymbol{u}^{k,n})-\dot{\boldsymbol{\gamma}}^{k,n}),$$

$$\boldsymbol{\sigma}_T^{k,n}=\boldsymbol{\sigma}_T^{k,n-1}-r_f(\boldsymbol{u}_T^{k,n}-\delta^{k,n}).$$

Solving the Stokes type problem at step 1 is a standard problem in fluid mechanics and many techniques are available for this (see for instance [59]). Here, $\mathcal{D}$ is discretized using a family of triangulations $(\mathcal{T}_h)_h$ made of finite elements ($h>0$ is the discretization parameter representing the greatest diameter of a triangle in $\mathcal{T}_h$). V_h is the FE space for the velocity field $\boldsymbol{u}^{k,n}$, W_h the FE space for the pressure field $p^{k,n}$, Q_h the FE space for the stresses deviators $\boldsymbol{\sigma}'^{k,n}$ and strain rate multipliers $\dot{\boldsymbol{\gamma}}^{k,n}$ and R_h the space for the for slip rate multipliers $\delta^{k,n}$ and tangential stresses $\boldsymbol{\sigma}_T^{k,n}$. Note that these finite element spaces cannot be chosen independently. For instance, in two dimensional computations, if V_h = [continuous P2] (i.e. the space of continuous functions which are second degree polynomials on each triangle), then we must choose W_h = [continuous P1], Q_h = [discontinuous P1] and R_h = [continuous P2]. This choice is used in all simulations presented in this paper.

Note that if convergence is achieved, then the iterative solution of the algorithm satisfies the nonlinear system (26)–(30). Indeed, if the convergence criterion $\boldsymbol{\sigma}'^{k,n}=\boldsymbol{\sigma}'^{k,n-1}, \boldsymbol{\sigma}_T^{k,n}=\boldsymbol{\sigma}_T^{k,n-1}$ is satisfied, then $\boldsymbol{D}(\boldsymbol{u}^{k,n})=\dot{\boldsymbol{\gamma}}^{k,n}$ and $\boldsymbol{u}_T^{k,n}=\delta^{k,n}$. From (33), we determine that the pair $\boldsymbol{D}(\boldsymbol{u}^{k,n})$ and $\boldsymbol{\sigma}'^{k,n}$ satisfies the flow rule (28) and the pair $\boldsymbol{u}_T^{k,n}$ and $\boldsymbol{\sigma}_T^{k,n}$ satisfies the friction law (20). Moreover we find that $\boldsymbol{D}(\boldsymbol{u}^{k,n})=\boldsymbol{D}(\boldsymbol{u}^{k,n-1})$, which means that $\boldsymbol{u}^{k,n}=\boldsymbol{u}^{k,n-1}$ and $\boldsymbol{u}^k=\boldsymbol{u}^{k,n}, \boldsymbol{\sigma}'^k=\boldsymbol{\sigma}'^{k,n}, \boldsymbol{\sigma}_T^k=\boldsymbol{\sigma}_T^{k,n}, p^k=p^{k,n}$ is a solution of (26)–(30).

References

[1] N. Brodu, P. Richard, R. Delannay, Shallow granular flows down flat frictional channels: steady flows and longitudinal vortices, Phys. Rev. E 87 (2013) 022202, http://dx.doi.org/10.1103/PhysRevE.87.022202.
[2] E.C. Bingham, Fluidity and Plasticity, Mc Graw-Hill, New-York, 1992.
[3] GDR MiDi group, On dense granular flows, Eur. Phys. J. E14 (2004) 341–365.
[4] C. Ancey, Plasticity and geophysical flows: a review, J. Non-Newton. Fluid Mech. 142 (2007) 4–35.
[5] B. Andreotti, Y. Forterre, O. Pouliquen, Les milieux granulaires, entre fluide et solide, Savoirs Actuels, EDP Sci. (2011).
[6] A. Mangeney, O. Roche, O. Hungr, O. Mangold, G. Faccanoni, A. Lucas, Erosion and mobility in granular collapse over sloping beds, J. Geophys. Res. – Earth Surf. 115 (2010) F03040.
[7] E. Lajeunesse, A. Mangeney-Castelnau, J.-P. Vilotte, Spreading of a granular mass on a horizontal plane, Phys. Fluids 16 (2004) 2371–2381.
[8] E. Lajeunesse, J.B. Monnier, G.M. Homsy, Spreading of a granular mass on a horizontal plane, Phys. Fluids 17 (2005) 103302.
[9] G. Lube, H.E. Huppert, R.S.J. Sparks, M. Hallworth, Axisymmetric collapse of granular columns, J. Fluid Mech. 508 (2004) 175.
[10] G. Lube, H.E. Huppert, R.S. Sparks, A. Freundt, Static and flowing regions in granular collapses down channels, Phys. Fluids 19 (2007) 043301.
[11] G. Lube, H.E. Huppert, R. Sparks, A. Freundt, Granular column collapses down rough, inclined channels, J. Fluid Mech. 675 (2011) 347–368.
[12] N.J. Balmforth, R.R. Kerswell, Granular collapse in two dimensions, J. Fluid Mech. 538 (2005) 399.
[13] S. Siavoshi, A. Kudrolli, Failure of a granular step, Phys. Rev. E 71 (2005) 051302.
[14] L. Lacaze, J. Phillips, R.R. Kerswell, Planar collapse of a granular column: experiments and discrete-element simulations, Phys. Fluids 20 (2008) 063302.
[15] A.J. Hogg, Two dimensional granular slumps down slopes, Phys. Fluids 19 (2008) 093301.
[16] M. Farin, A. Mangeney, O. Roche, Fundamental changes of granular flow dynamics, deposition, and erosion processes at high slope angles: insights from laboratory experiments, J. Geophys. Res. Earth Surf. 119 (2014) 504–532.
[17] G.B. Crosta, S. Imposimato, D. Roddeman, Numerical modeling of 2-D granular step collapse on erodible and non-erodible surface, J. Geophys. Res. 114 (2009) F03020, http://dx.doi.org/10.1029/2008JF001186.
[18] A. Mangeney-Castelnau, F. Bouchut, J.-P. Vilotte, E. Lajeunesse, A. Aubertin, M. Pirulli, On the use of Saint-Venant equations to simulate the spreading of a granular mass, J. Geophys. Res. 110 (2005) B09103, http://dx.doi.org/10.1029/2004JB003161.
[19] R.R. Kerswell, Dam break with coulomb friction: a model for granular slumping, Phys. Fluids 17 (2005) 057101.
[20] E. Larrieu, L. Staron, E.J. Hinch, Raining into shallow water as a description of the collapse of a column of grains, J. Fluid Mech. 554 (2006) 259.
[21] E.E. Doyle, H.E. Huppert, G. Lube, H.M. Mader, R.S.J. Sparks, Static and flowing regions in granular collapses down channels: Insights from a sedimenting shallow water model, Phys. Fluids 19 (2007) 106601.
[22] L. Staron, E.J. Hinch, Study of the collapse of granular columns using 2D discrete-grains simulation, J. Fluid Mech. 545 (2005) 1.
[23] R. Zenit, Computer simulations of the collapse of a granular column, Phys. Fluids 17 (2005) 031703.
[24] L. Girolami, V. Hergault, G. Vinay, A. Wachs, A three-dimensional discrete-grain model for the simulation of dam-break rectangular collapses: comparison between numerical results and experiments, Granul. Matter 14 (2012) 381–392.
[25] L. Lacaze, R.R. Kerswell, Axisymmetric granular collapse: a transient 3D flow test of viscoplasticity, Phys. Rev. Lett. 102 (2009) 108305.
[26] C. Meruane, A. Tamburrino, O. Roche, On the role of the ambient fluid on gravitational granular flow dynamics, J. Fluid Mech. 648 (2010) 381.
[27] P.-Y. Lagrée, L. Staron, S. Popinet, The granular column collapse as a continuum: validity of a two-dimensional Navier–Stokes model with a $\mu(I)$-rheology, J. Fluid Mech. 686 (2011) 378–408.
[28] I.R. Ionescu, Viscoplastic shallow flow equations with topography, J. Non-Newton. Fluid Mech. 193 (2013) 116–128.
[29] L.E. Silbert et al., Granular flow down an inclined plane: Bagnold scaling and rheology, Phys. Rev. E 64 (2001) 051302.
[30] P. Jop, Y. Forterre, O. Pouliquen, Crucial role of sidewalls in dense granular flows: consequences for the rheology, J. Fluid Mech. 541 (2005) 167–192.
[31] P. Jop, Y. Forterre, O. Pouliquen, A constitutive law for dense granular flows, Nature 441 (2006) 727–730.
[32] O. Cazacu, I.R. Ionescu, Compressible rigid visco-plastic fluids, J. Mech. Phys. Solids 54 (2006) 1640–1667.
[33] I.R. Ionescu, Onset and dynamic shallow flow of a viscoplastic fluid on a plane slope, J. Non-Newton. Fluid Mech. 165 (19-20) (2010) 1328–1341.
[34] P. Perzyna, Fundamental problems in viscoplasticity, in: H.L. Dryden (Ed.), Advances In Applied Mechanics, 9, Academic Press, 1966, pp. 243–377.
[35] G. Duvaut, J.-L. Lions, Les inéquations en mécanique et en physique, Dunod, Paris, 1972.
[36] D.C. Drucker, W. Prager, Soil mechanics nd plastic analysis of limit design, Quart. Appl. Math. 10 (1952) 157–175.
[37] S.B. Savage, The mechanics of rapid granular flows, Adv. Appl. Mech. 24 (1984) 289–366.
[38] C. Ancey, P. Coussot, P. Evesque, A theoretical framework for very concentrated granular suspensions in steady simple shear flow, J. Rheol. 43 (1999) 1673–1699.
[39] O. Pouliquen, Y. Forterre, Friction law for dense granular flows: applications to the motion of a mass down a rough inclined plane, J. Fluid Mech. 453 (2002) 133–151.
[40] N. Taberlet, P. Richard, A. Valance, R. Delannay, W. Losert, J.M. Pasini, J.T. Jenkins, Super stable granular heap in thin channel, Phys. Rev. Lett. 91 (2003) 264301.
[41] F. Bouchut, R. Eymard, A. Prignet, Convergence of conforming approximations for inviscid incompressible Bingham fluid flows and related problems, J. Evol. Eq. 14 (2014) 635–669.
[42] C. Lusso, Modélisation numérique des écoulements gravitaires viscoplastiques avec transition fluide/solide, PhD thesis, Université Paris-Est, Champs-sur-Marne, 2013.
[43] F. Hecht, New development in freefem++, J. Numer. Math. 20 (2012) 251–265.
[44] Martin Rentschler, PhD, 2009.
[45] C. Meriaux, Two dimensional fall of granular columns controlled by slow horizontal withdrawal of a retaining wall, Phys. Fluids 18 (2006) 093301.
[46] P. Saramito, N. Roquet, An adaptive finite element method for viscoplastic fluid flows in pipes, Comput. Methods Appl. Mech. Eng. 190 (2001) 5391–5412.
[47] O. Cazacu, I.R. Ionescu, T. Perrot, Steady-state flow of compressible rigid-viscoplastic media, Int. J. Eng. Sci. 44 (2006) 1082–1097.
[48] E.L. Thompson, H.E. Huppert, Granular column collapses: further experimental results, J. Fluid Mech. 575 (2007) 177–186.
[49] A. Lucas, A. Mangeney, J.-P. Ampuero, Frictional weakening in landslides on Earth and on other planetary bodies, Nat. Commun. 5 (2014) 3417.
[50] F. Bouchut, I.R. Ionescu, and A. Mangeney, An analytic approach for the evolution of the static-flowing interface in viscoplastic granular flows, 2014.
[51] C. Lusso, F. Bouchut, A. Ern, A. Mangeney, A Simplified Model of Thin Layer Static/Flowing Dynamics for Granular Materials with Yield, submitted for publication (2014).
[52] R. Glowinski, P. Le Tallec, Augmented Lagrangian and Operator Splitting method in Non-Linear Mechanics, SIAM Stud. Appl. Math. (1989).
[53] M. Fortin, R. Glowinski, Méthodes de Lagrangien augmenté, application à la résolution de problèmes aux limites, Dunod, 1982.
[54] I.R. Ionescu, Augmented Lagrangian for shallow viscoplastic flow with topography, J. Comput. Phys. 242 (2013) 544–560.
[55] T. Hughes, W. Liu, T. Zimmermann, Lagrangian–Eulerian finite element formulation for incompressible viscous flows, Comput. Methods Appl. Mech. Eng. 29 (1981) 329–349.
[56] B. Maury, Characteristics ALE method for the unsteady 3D Navier–Stokes equations with a free surface, Int. J. Comput. Fluid Dyn. 6 (1996) 175–188.
[57] V. Maronnier, M. Picasso, J. Rappaz, Numerical simulation of three dimensional free surface flows, Int. J. Numer. Method Fluids 42 (2003) 697–716.
[58] F. Duarte, R. Gormaz, S. Natesan, Arbitrary Lagrangian–Eulerian method for Navier–Stokes equations with moving boundaries, Comput. Methods Appl. Mech. Eng. 193 (2004) 4819–4836.
[59] O. Pironneau, Finite Element Methods for Fluids, John Wiley & Sons Ltd., Chichester, 1989.
[60] K. Kelfoun, T.H. Druitt, Numerical modeling of the emplacement of Socompa rock avalanche, Chile, J. Geophys. Res. 110 (2005) B12202.